Acylation of MLKL impacts its function in necroptosis

Apoorva J. Pradhan,[1] Shweta Chitkara,[1] Ricardo X. Ramirez,[2] Viviana Monje-Galvan,[2] Yasemin Sancak,[3] G. Ekin Atilla-Gokcumen[1]*

[1] Department of Chemistry, University at Buffalo, The State University of New York, Buffalo, New York 14260, USA

[2] Department of Chemical and Biological Engineering, University at Buffalo, The State University of New York, Buffalo, New York 14260, USA

[3] Department of Pharmacology, University of Washington, Seattle, Washington 98195, USA

*Corresponding author: ekinatil@buffalo.edu

ABSTRACT

Mixed lineage kinase domain-like (MLKL) is a key signaling protein of necroptosis. MLKL oligomerizes and translocates to the plasma membrane upon phosphorylation by the necrosome. At the plasma membrane, MLKL induces membrane permeabilization which contributes to the inflammatory activity of necroptosis. Membrane binding of MLKL oligomers is initially initiated by the electrostatic interaction between the protein and membrane phospholipids. We have previously showed that MLKL and its phosphorylated form (pMLKL) are *S*-acylated during necroptosis and that this acylation increases their membrane binding. In this work, we characterize acylation sites of MLKL and identify multiple cysteines that can undergo acylation with an interesting promiscuity at play. Our results show that MLKL and pMLKL undergo monoacylation, with C184, C269 and C286 being the possible acylation sites. In other words, while there are multiple cysteines that are accessible for acylation, the acylation predominantly occurs at a single cysteine. The molecular interactions that determine the exact acylation site remain unclear. Investigating the *S*-palmitoyltransferases that might acylate MLKL in necroptosis, we showed that zDHHC21 activity has the strongest effect on pMLKL acylation and reducing the activity of zDHHC21 significantly improved membrane integrity of necroptotic cells. We also observed that inactivation of zDHHC21 reduced the pMLKL levels in the cells, suggesting that blocking the acylation of pMLKL results in reduced membrane binding, destabilization of the protein at the membrane interface and cause its degradation. Finally, through molecular dynamics simulations, we verify the acyl tail of MLKL can insert into the membrane and causes conformational changes to the protein and lipid re-organization of the membrane. At a broader level, our findings shed light onto pMLKL processing and the effect of *S*-acylation on pMLKL functioning in necroptosis.

INTRODUCTION

Different types of programmed cell deaths follow complex and interconnected signaling networks and play different roles in cellular homeostasis and pathological conditions (Green, 2022; Gibellini and Moro, 2021). Necroptosis is one such type of programmed cell death that is characterized by cell swelling, disruption of plasma membrane and release of intracellular contents resulting in extensive inflammatory activity (Vandenabeele et al., 2010; Kaczmarek et al., 2013). Although these morphological characteristics are similar to those in necrosis, which is not regulated, necroptosis has a distinct molecular mechanism. The inflammatory nature of necroptosis is due to membrane rupture and leakage of intracellular contents and is triggered by the activation of the tumor necrosis factor (TNF) receptors via TNF family of cytokines (Molnár et al., 2019). Binding of TNF alpha (TNFα) to TNF receptor recruits multiple adaptor proteins, one of which is receptor interacting protein kinase 1 (RIPK1). This event can signal a cell survival pathway or a cell death pathway such as apoptosis when caspase-8 activity is high. Sustained presence of RIPK1 and decreased caspase-8 activity initiates necroptosis where RIPK1 forms a complex with RIPK3, followed by autophosphorylation of RIPK3 (Gough and Myles, 2020). This complex results in the phosphorylation of mixed lineage kinase domain-like (MLKL) which then oligomerizes and translocates to the plasma membrane causing membrane rupture. These key interactions that result in the eventual membrane permeabilization make MLKL the executioner protein of necroptosis (Murphy et al., 2013; Wang et al., 2014; Chen et al., 2014; Liu et al., 2017).

MLKL consists of a N-terminal four-helix bundle domain (4HB) with two additional helices (brace domain) connecting the 4HB to the C-terminal pseudokinase domain (Murphy et al., 2013). The 4HB consists of multiple positively charged amino acids that can interact with the negatively charged phosphatidylinositol phosphates (PIP) at the plasma membrane (Dondelinger et al., 2014; Quarato et al., 2016). This protein-lipid interaction is essential for MLKL binding to the plasma membrane. The interactions between the C-terminal helix of the brace with the rest of the helices can inhibit the functioning of MLKL in necroptosis (Su et al., 2014). The helices of the brace are responsible for oligomerization of MLKL and also maintain contacts between the 4HB and the pseudokinase domain after phosphorylation, communicating the conformational changes within the pseudokinase domain to the 4HB (Quarato et al., 2016; Davies et al., 2018; Su et al., 2014). Work by Wang *et al.* and Dondelinger *et al.* have suggested that the membrane disruptive activity of MLKL results from the interactions between the positively charged residues in the 4HB and the negatively charged PIPs species present in the membrane leaflet by liposomal models (Dondelinger et al., 2014; Wang et al., 2014). Similarly, Su *et al.*, using reconstituted membranes,

have suggested that the 4HB can directly insert into the membranes, causing membrane distruption (Su et al., 2014).

The C-terminal of MLKL is a pseudokinase; while it can bind to ATP, it lacks kinase activity due to the absence of Mg^{+2} binding site necessary for catalysis (Murphy et al., 2013). Multiple studies implicate the pseudokinase domain functioning as a 'switch' to regulate necroptotic signaling, downstream of MLKL phosphorylation with several charged residues within the domain essential for driving the oligomerization and translocation to the plasma membrane (Petrie et al., 2018; Hildebrand et al., 2014). A study further elucidated the sequence of MLKL activation by proposing a model of initial dimerization of the pseudokinase domain after phosphorylation by RIP3 followed by oligomerization via the brace region (Zhang et al., 2021). Overall, the functioning of MLKL as the executioner of necroptosis involves multiple features and dynamic changes that warrants further investigations.

Previous studies from our lab revealed additional protein-membrane interactions that mediate MLKL binding to the plasma membrane. Using untargeted lipidomics, we demonstrated that very long chain fatty acids (fatty acids with ≥ 20 carbons) (Guillou et al., 2010) accumulate downstream of RIPK1 activation (Parisi et al., 2017) and contribute to the destabilization of the plasma membrane (Parisi et al., 2019). We also showed that incorporation of very long chain fatty acids to MLKL and pMLKL increases their membrane binding and exacerbates membrane permeabilization during necroptosis (Pradhan et al., 2021). Biochemical characterizations demonstrated that acylation of MLKL and pMLKL is *S*-linked and occurs at the plasma membrane, in part mediated by palmitoyltransferase zDHHC5, during necroptosis. In this work, we studied the involvement of other palmitoyl transferases in the acylation of MLKL and pMLKL during necroptosis, identified cysteines that undergo acylation during necroptosis and investigated the impact of acylation on protein stabilization in this process. First, using all atom molecular dynamics simulations, SwissPalm predictions and cysteines with previously unaccounted-for functions, we prioritized cysteines that are likely to interact with the lipid bilayer since palmitoyl transferases are membrane-associated. Mutagenesis experiments followed by acyl-PEG exchange (APE) suggested that C184, C269 and C286 can undergo acylation in necroptosis. Further, we investigated the role of different zDHHCs in the acylation of MLKL and pMLKL in necroptosis and show that disrupting the zDHHC21-mediated acylation of pMLKL ameliorates plasma membrane permeabilization in this process. We also show that inactivation of zDHHC21 decreases overall levels of pMLKL, most likely through increased protein degradation. Together, these studies help to establish deeper insights into interactions and structural features of pMLKL

affecting its membrane association and demonstrate that membrane binding of pMLKL and its retention at the plasma membrane stabilizes the protein levels during necroptosis, contributing to membrane disruption.

RESULTS

C184, C269 and C286 of MLKL are acylated in necroptosis. Our previous efforts to understand protein acylation in necroptosis showed that MLKL and pMLKL undergo *S*-linked acylation during necroptosis downstream of plasma membrane translocation. Our results also showed that these proteins are predominantly monoacylated during necroptosis (Pradhan et al., 2021). The human MLKL has 10 cysteines across the 4HB, the brace and the pseudokinase domain, with C18, C24, C28 and C86 within the 4HB; C184 in the brace helix and C269, C286, C415, C437 and C448 within the pseudokinase domain (**Figure 1A**) (Petrie et al., 2020). The four cysteines in the 4HB, C18, C24, C28 and C86 are involved in oligomerization of MLKL and induction of necroptosis (Liu et al., 2017). Hence, it is likely that they are buried in the oligomerization interface and are not accessible to palmitoyltransferases located at the plasma membrane. Further, studies report that C86 is the target residue of necrosulfonamide which inhibits MLKL oligomerization (Sun et al., 2012; Huang et al., 2017a), supporting that C86 is not likely to interact with the plasma membrane and be available for acylation. Based on these, we decided to interrogate the remaining cysteines for acylation targets in necroptosis.

We first used all-atom molecular dynamic simulations to investigate the interaction of murine MLKL with a membrane model based on the lipid content of HT-29 cells (Ramirez et al., 2023). The simulations identified different protein-bound conformations with the 4HB or the pseudokinase domain interacting with the lipid membrane; the 4HB was found to have deeper membrane insertion, in agreement with previously published reports of the 4HB being responsible for contact with the lipid membrane and subsequent insertion (Su et al., 2014). The trajectories showing interaction of the pseudokinase domain with the membrane resulted in a different lipid landscape around the protein after the simulation reached equilibrium (Ramirez et al., 2023). Upon further examination of these trajectories, we observed C23, C379, C280 and C407 consistently have the highest occupancy in terms of percentage of time bound to the membrane (**Table S1**, highlighted in green). The corresponding cysteines in human MLKL were then selected for further investigations ($C18_{human} \rightarrow C23_{murine}$, $C286_{human} \rightarrow C280_{murine}$, $C415_{human} \rightarrow C407_{murine}$; $Y387_{human} \rightarrow C379_{murine}$ in MLKL, **Figure 1A**, **Figure S1A**). in parallel, we consulted with SwissPalm database (Blanc et al., 2019, Blanc et al., 2015) which predicts C18 and C24 to be

palmitoylated. The remaining cysteines, C184, C269, C437 and C448, do not have any known role in MLKL functionality in necroptosis. Based on our simulation results, SwissPalm predictions and literature information available, we shortlisted C18, C24, C184, C269, C286, C415, C437 and C448 to be investigated for their role in acylation of MLKL in necroptosis.

We conducted mutagenesis studies to investigate the involvement of the above-mentioned cysteines in pMLKL and MLKL acylation during necroptosis. We first subcloned a commercially available MLKL sequence in a pLYS1 vector expressing a Myc tag and introduced point mutations to generate $MLKL_{C18S}$, $MLKL_{C24S}$, $MLKL_{C184S}$, $MLKL_{C269S}$, $MLKL_{C415S}$, $MLKL_{C437S}$ and $MLKL_{C448S}$ constructs. These were then used to generate lentiviruses to transduce HT-29 cells and express Myc-tagged WT MLKL (WT-MLKL) and mutant forms of MLKL. We confirmed the expression of WT-MLKL and mutant forms and the ability of the HT-29 cells expressing Myc-tagged MLKL forms to undergo necroptosis by Western blotting (**Figure 1B**). Briefly, we induced necroptosis using BV6, a SMAC mimetic and a pan-caspase inhibitor zVAD-FMK followed by TNF-α. We collected cells after 3 h of necroptosis induction and samples were analyzed using Western blotting. The two bands in Figure 1B correspond to the endogenous MLKL (lower band, MW: ~55 kDa) and the Myc-tagged MLKL (upper band, MW: ~57 kDa). Both WT and mutant forms of MLKL can undergo acylation in necroptosis, supporting that the mutation of C to S does not impact necroptotic signaling or MLKL functionality (**Figure 1B**). We further confirmed the ability of Myc-tagged WT-MLKL to undergo acylation during necroptosis by using a clickable C20 FA probe as we described in an earlier work (**Figure 1C**) (Pradhan et al., 2021). These results established that Myc-tagged MLKL can undergo acylation similar to the endogenous MLKL in necroptosis.

We then used APE to study the role of these cysteines on the extent of acylation of MLKL. APE involves removing the acyl chains on modified cysteines with hydroxylamine to generate free sulfhydryl groups and then tagging these sulfhydryl groups with a high molecular weight polyethylene glycol (PEG) which introduces a mass shift that can be observed using SDS-PAGE (Percher et al., 2017). This allows to calculate the extent of acylation for the mutants by comparing the levels of acylated Myc-tagged MLKL to the level of non-acylated Myc-tagged MLKL expressed in the cells, for control WT-MLKL and each of the mutants. We observed that three mutant forms of MLKL, $MLKL_{C184S}$, $MLKL_{C269S}$ and $MLKL_{C286S}$, showed a significant decrease ($p < 0.05$, t-test) in acylation as compared to WT-MLKL (**Figure 1D-E**). Specifically, C184S and C269S mutations resulted in a 68% and 65% reduction whereas C286S mutation showed a 53% reduction in

acylation of MLKL-myc. We note that the C24S mutant also showed ~20-30% reduction in acylation but this reduction was not statistically significant ($p > 0.05$).

While our previous results suggest the involvement of a single cysteine residue involved in the acylation of MLKL during necroptosis, our mutagenesis results point to a possible preference of C184, C269 and C286 as acylation substrates. C184 is situated in the brace helix of MLKL, with the other two cysteines in the pseudokinase domain (Petrie et al., 2020) with the brace in mouse MLKL found to interact with membrane lipids (Sethi et al., 2022). Our results suggest a mechanism where acylation of either of the three cysteines during necroptosis, locks the protein in a specific conformation at the membrane surface upon insertion of the acylated tail, with the other two cysteines being unmodified.

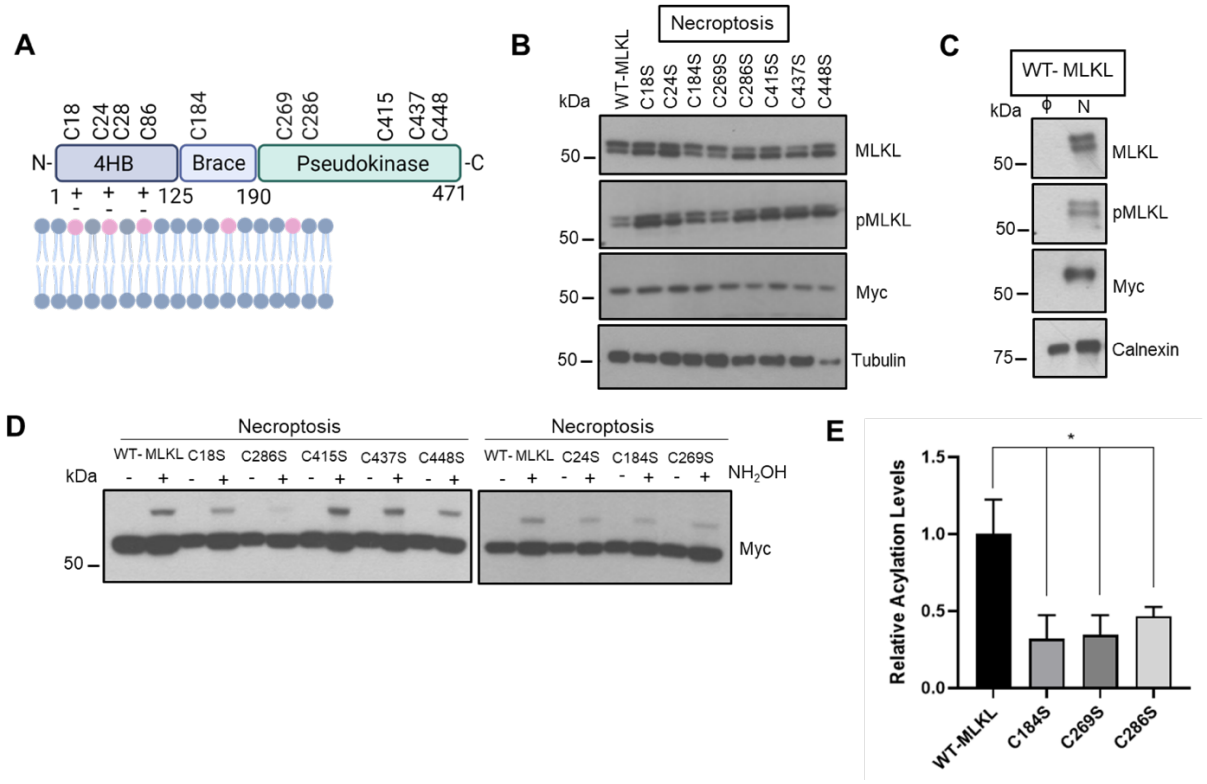

Figure 1: Acylation of cysteines in MLKL. (A) Representation of human MLKL showing the N-terminal 4-helix bundle (4HB) connected to the C-terminal pseudokinase domain via the two helix brace. 4HB spans from amino acid residues 1-125, brace helices upto residue 190 and the pseudokinase domain till residue 471.(Petrie et al., 2020) The positively charged residues in the 4HB interact with the negatively charged PIPs (shown in pink) via electrostatic interactions. The ten cysteines present in human MLKL and their location have been shown. The cysteines 184, 269 and 286 which show acylation in our experiments have been marked in red. **(B)** Western blot analysis of Myc-tagged WT-MLKL and the 8 constructs with C to S mutations. Necroptosis was induced in HT-29 cells following treatment with 1 μM BV6, 25 μM zVAD-fmk and 10 ng/μL TNFα and collected after 3h. Each of the constructs expresses the Myc-tagged MLKL and also

undergoes necroptosis. MLKL and pMLKL show up as two bands with the Myc-tagged form being the top band and endogenous forms being the bottom bands. **(C)** WT-MLKL control and necroptotic cells were treated with C20 alkFA and fractionated. The membrane fraction was subjected to CuAAC to attach biotin-azide followed by enrichment on neutravidin resin. The samples were blotted for MLKL, pMLKL and Myc. Calnexin was used as loading control. **(D)** C184S, C269S and C286S show profound reduction in acylation as compared to WT-Myc in necroptosis. Acyl PEG exchange with N-ethylmaleimide (NEM), hydroxylamine (NH_2OH) and methoxypolyethylene glycol maleimide (mPEG-Mal) was performed on necroptotic WT-MLKL and cysteine mutant cells. The conditions without NH_2OH (represented by -) are controls for presence of acylation. The samples are blotted for myc. **(E)** Quantification of the extent of acylation for C184S, C269S and C286S with respect to control WT-myc. The extent of acylation is calculated by dividing the background-subtracted intensities of migrated Myc-tagged MLKL relative to non-migrated Myc-tagged MLKL for WT-Myc and C184S, C269S and C286S (using Fiji). The relative values are calculated by normalizing values for the mutants with respect to the values obtained for Myc-tagged WT-MLK. Data represent the mean ± 1 SD; n=3. * represents $p < 0.05$

Acylated MLKL interacts with membrane lipids. In our previous work, we simulated a complex membrane model composed of a mixture of 5 lipid species [dioleoyl-phosphatidylcholine (DOPC), dioleoyl-phosphatidylethanolamine (DOPE), Cholesterol, palmitoyl-oleoyl-phosphatidylinositol 4-phosphate (PIP), palmitoyl-oleoyl-phosphatidylinositol (2,5)-bisphosphate (PIP_2)] with the murine MLKL protein (PDBID: 4BTF). We showed that MLKL interacts with membrane lipids and leaves a specific fingerprint on the membrane local composition upon binding. Here, we extend the simulations to a sample system comprised of an *S*-acylated MLKL with C24 FA at C286 (residue 280 in murine MLKL) and the same membrane model. We simulated a total of three replicas referred to as 280r1, 280r2, and 280r3. We characterized protein-lipid interactions and compared these observations with our experiments and previous simulation trajectories to assess the effect of acylation in MLKL-membrane interaction.

Figure 2A-B show the protein starting from a bound conformation with the acylated tail partially or fully inserted into the membrane, and the final bound conformations, respectively. The lipid tail remains inserted during the full trajectory for 280r1 and 280r2, whereas it reverts to a hydrophobic pocket in the protein around 250ns in replica 280r3. The most notorious difference between the acylated system and that of the endogenous MLKL in our previous study (Ramirez et al., 2023) is the conformational change of the protein in 280r2 and 280r3. In these replicas, 4HB (shown in blue) shifts its original position and aligns with the brace in a parallel fashion (shown in red), which did not occur in the non-acylated version. In all our simulation trajectories, we observe characteristic profiles for the protein-lipid frequency of contact depending on the specific protein domain that interacts with the membrane (**Figure 2C**). The conformational changes observed in the 4HB and brace conformational changes appear to result from the

insertion and interaction of the acyl tail and other membrane lipids (**Figure 2D**). When inserted into the membrane, the 24-carbon acyl tail behaves like other lipids in the membrane and influences the lateral distribution of lipids nearby, which in turn modulates protein conformational changes on the surface. The interplay between protein and lipids is highly dynamic and can result in protein conformational changes that pull the acyl tail from the membrane temporarily, as in 280r3 (**Figure 2B**). It is plausible that a local lipid environment rich in VLCFAs would provide a more hydrophobic environment to stabilize the inserted acyl tail and promote membrane disruption. Alternatively, when more MLKL units are present, conformational changes observed in the simulation of the monomer may not occur simply due to steric effects.

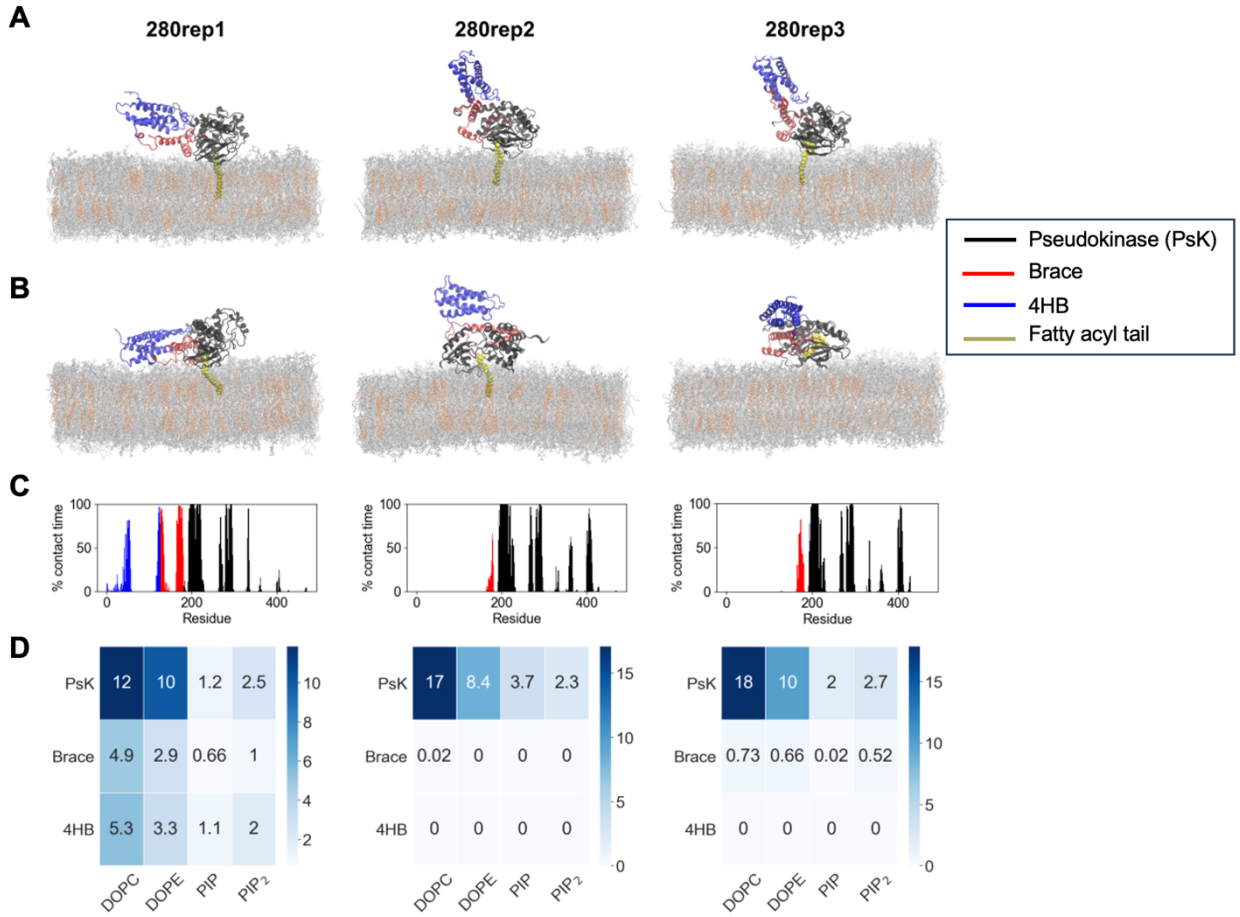

Figure 2: Molecular dynamics shows interaction of acylated MLKL with membrane lipids. (A) Position of the protein in the membrane after 50ns of equilibration, initial interaction; (**B**) after 1050ns of simulation; (**C**) Frequency of contact of each residue in the protein during the simulation; (**D**) Mean lipid distribution of the lipids within 12 Å of the protein for the last 200ns of simulation.

Acylation of MLKL is mediated by zDHHC family of protein transferases. We have previously shown that blocking phosphorylation and oligomerization and translocation of MLKL prevents its acylation during necroptosis, strongly suggesting that the acylation occurs at the plasma membrane downstream to its phosphorylation and oligomerization. In the same study, focusing on palmitoyl *S*-transferases that are known to localize at the plasma membrane and have been shown to be involved in membrane dynamics such as remodeling and endocytosis, we initially targeted zDHHC5 (Ohno et al., 2006; He et al., 2014; Hilgemann et al., 2013). We showed that knocking down zDHHC5 reduced the acylation of MLKL and pMLKL but did not completely block it, suggesting that there might be other acyltransferases at the plasma membrane that are involved in the acylation of MLKL and pMLKL during necroptosis (Pradhan et al., 2021).

The zDHHC family of palmitoyltransferases consists of 23 members residing mainly at the endoplasmic reticulum and Golgi with a few localized to the plasma membrane and the mitochondria (Jiang et al., 2018). These enzymes consist of four transmembrane domains and a conserved cysteine-rich domain with the Asp-His-His-Cys (DHHC) active site. The cysteine-rich domain binds Zn^{+2} making zDHHCs, zinc finger proteins (Rana et al., 2018). While Zn^{+2} does not coordinate with the active cysteine residue in catalysis, they have been shown to play a role in maintaining the stability of the enzyme as well as interacting with residues that might be involved in the positioning of the catalytic cysteine (Gottlieb et al., 2015). The cysteine-rich domain with the active site and the N- and the C-terminus are cytosolic. Apart from the cysteine-rich domain, there are some other amino acid sequences amongst the different zDHHCs which might play a role in substrate recruitment (Plain et al., 2017; Plain et al., 2020). These enzymes can exhibit a certain degree of substrate specificity although some redundancies have also been observed. Similar to substrate specificity, zDHHCs also exhibit fatty acyl-CoA specificity. While some members are more promiscuous in their fatty acyl-CoA preference, certain zDHHCs are more specific (Jiang et al., 2018; Greaves et al., 2017). Based on the crystal structure of zDHHC20 and the subsequent proposed mechanism of acylation, the transmembrane domains form a hydrophobic cavity which serves to hold the fatty acyl CoA substrate (Rana et al., 2018). Specific amino acid residues in the transmembrane domains that make up this cavity affect the length of fatty acyl CoA that can be accommodated (Jennings and Linder, 2012; Greaves et al., 2017). The catalytic mechanism involves two steps with the first being a rapid autoacylation of the Cys in the DHHC followed by the slower transfer of the acyl group to the protein substrate (Rana et al., 2018).

Based on the promiscuity and multiple domains impacting substrate recognition, it is difficult to predict protein substrate specificity using bioinformatic tools. Here, we took a systematic approach to fully characterize the zDHHC family of proteins involved in acylation of MLKL and pMLKL in necroptosis. We were especially interested in the zDHHC members that localize at the plasma membrane, similar to zDHHC5, based on our previous finding that acylation of MLKL and pMLKL take place at the plasma membrane. Different studies also implicate zDHHC20 and zDHHC21 to be localized at the plasma membrane (Ohno et al., 2006). In parallel to cellular localization, we looked at the gene expression profiles of the different zDHHCs in HT-29 cells using a transcriptomic dataset we have recently reported, to confirm the expression of the plasma membrane-associated zDHHC20 and zDHHC21 in HT-29, our model cell line of necroptosis (Lu et al., 2023). This analysis showed that zDHHC5 had the highest level of expression followed by zDHHC20, with zDHHC21 accounting for ~2% of all the zDHHC transcripts (**Figure 3A**). Based on the expression analysis in HT-29 cell line and subcellular localization of the zDHHCs, we decided to investigate the role of zDHHC20 and zDHHC21 in parallel to zDHHC5 in acylation of MLKL and pMLKL in necroptosis. We knocked down these zDHHCs using shRNA (**Figure 3B**, shzDHHC5, shzDHHC20, shzDHHC21; shRFP was used a negative control). We achieved efficient knockdown of the protein expression of zDHHC5, zDHHC20 and zDHHC21, with a knockdown efficiency of ~70% for shzDHHC5 and 21 and ~90% for shzDHHC20 (**Figure 3B**).

We then investigated the effect of reduced zDHHC5, 20 and 21 activities on the acylation of MLKL and pMLKL in necroptosis using APE. We induced necroptosis in shzDHHC5, shzDHHC20, shzDHHC21 and shRFP cells. We compared the intensities of non-acylated-MLKL and -pMLKL (lower band) and their acylated form (migrated, upper bands, indicated by black arrows, **Figure 3C**). We quantified the difference in acylation between the knockdowns by calculating the ratios of the migrated band intensities of MLKL and pMLKL with the respective non-migrated band intensities. We observed a significant decrease in acylation of both MLKL and pMLKL in shzDHHC5 and shzDHHC21 cells. MLKL showed 30% and 59% reduction in acylation in shzDHHC5 and shzDHHC21 cells; while pMLKL was reduced 18% and 53%, respectively ($p < 0.05$, t-test; see **Figure 3C** for a representative Western blot image; quantifications of Western blots are shown in **Figure 3D-E**). Overall, the knockdown of zDHHC21 had a more profound effect in reducing the acylation of MLKL and pMLKL as compared to zDHHC5. The knockdown of zDHHC20 had no significant effect on acylation of MLKL and pMLKL in necroptosis albeit efficient knockdown levels (**Figure S2A-B,** $p > 0.05$, t-test), supporting that zDHHC20 does not play a role in acylation of pMLKL and MLKL in necroptosis.

Acylation of MLKL and pMLKL exacerbates membrane permeability during necroptosis (Pradhan et al., 2021). Therefore, we wanted to investigate if a link exists between the zDHHC-mediated acylation and membrane permeabilization observed during necroptosis. To that effect, we tested whether the activities of zDHHC5 and 21 have an impact on membrane permeabilization, by propidium iodide (PI) uptake, in necroptosis. We observed a ~40% and 60% reduction in PI uptake which indicated reduced membrane permeability in shzDHHC5 and shzDHHC21 cells, respectively ($p<0.05$ for shzDHHC5 and $p<0.01$ for shzDHHC21, **Figure 3F**). The knockdown of zDHHC20 had no appreciable effect on membrane permeability in necroptotic cells as compared to control counterparts (**Figure 3F**), consistent with the lack of effect of shzDHHC20 in pMLKL and MLKL acylation (**Figure S2**). Overall, these results suggest that zDHHC5 and 21 are involved in the acylation of MLKL and pMLKL at the plasma membrane during necroptosis and contribute to the membrane permeabilization in this process.

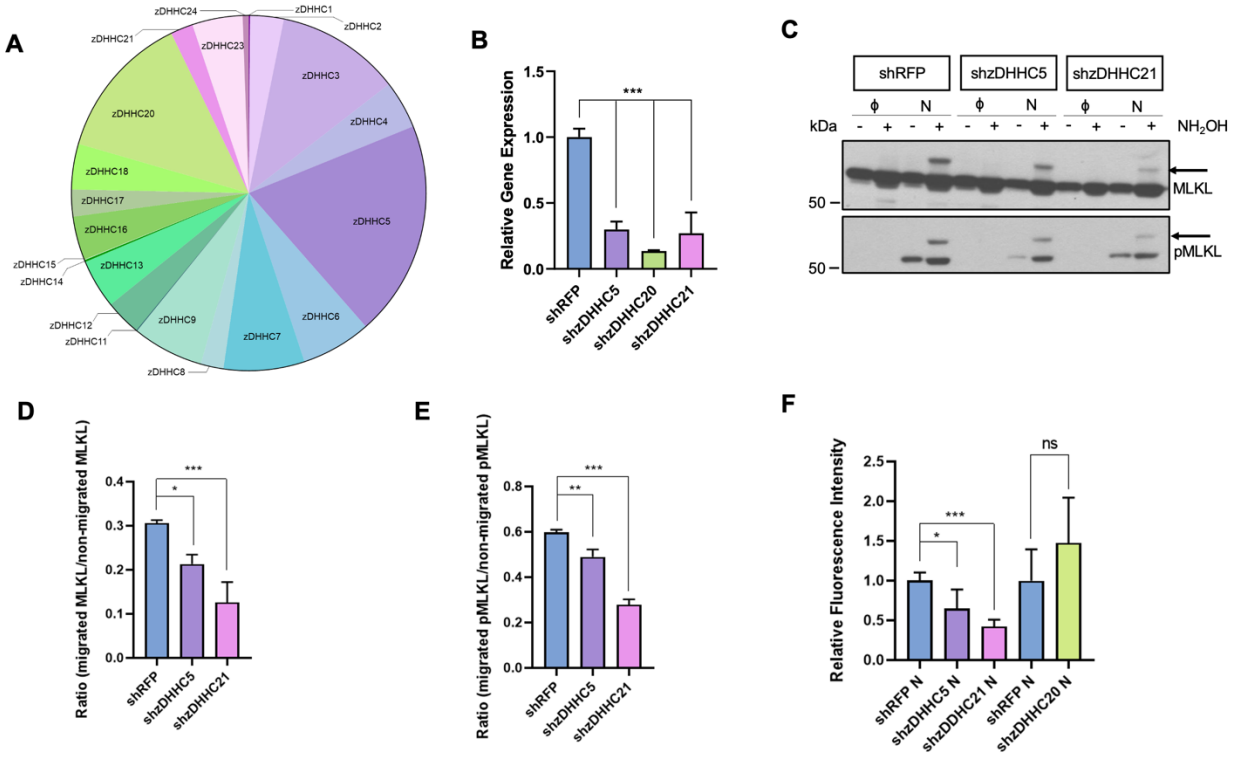

Figure 3: zDHHC family of enzymes regulate acylation of MLKL and pMLKL in necroptosis. (**A**) Pie chart representing expression levels of the zDHHC palmitoyl transferases in HT-29.(Lu et al., 2023) (**B**) Gene expression levels indicating knockdown of zDHHC5, zDHHC21 and zDHHC20. We knocked down zDHHC5, zDHHC21 and zDHHC20 using a lentiviral shRNA vector in HT-29. Relative gene expression levels are calculated as ratio of expression level of each target gene compared to the control HPRT1 expression levels. Data represent mean ± 1 SD; n=3. *** represents $p < 0.001$. (**C**) Acyl PEG exchange with NEM, NH_2OH and mPEG-Mal in control and necroptotic shRFP, shzDHHC5 and shzDHHC21 cells. The conditions without NH_2OH (represented by -) are controls for presence of acylation. The samples are blotted for MLKL and pMLKL. (**D**) Quantification of acylated MLKL in shzDHHC5 and shzDHHC21 compared to shRFP.

The ratio is calculated by dividing migrated band intensities of MLKL with non-migrated band intensities. Data represent mean ± 1 SD; n=3. * represents $p < 0.05$, *** represents $p < 0.001$. (**E**) Quantification of acylated pMLKL in shzDHHC5 and shzDHHC21 compared to shRFP. The ratio is calculated by dividing migrated band intensities of pMLKL with non-migrated band intensities. Data represent mean ± 1 SD; n=3. ** represents $p < 0.01$, *** represents $p < 0.001$. (**F**) zDHHC knockdown affects membrane permeabilization. Relative fluorescence intensity represents the propidium iodide uptake of shzDHHC cells compared to control shRFP cells in necroptosis. Data represent mean ± 1 SD; n=4. * represents $p < 0.05$, *** represents $p < 0.001$.

zDHHC21 activity regulates the levels of pMLKL during necroptosis. Previous studies showed that zDHHC21 depletion ameliorated septic injury in renal reperfusion (Yang et al., 2021) and barrier dysfunction in endothelial inflammation (Beard et al., 2016), suggesting a role for zDHHC21 in membrane integrity. This role of zDHHC21 is consistent with our observations of increased membrane integrity (**Figure 3F**) and reduced pMLKL acylation in shzDHHC21 cells during necroptosis (**Figure 3C-E**). Based on these, we decided to focus on the role of zDHHC21 in the fate of pMLKL, the functional form of MLKL in necroptosis, especially in the context of pMLKL maintained in cells, its membrane recruitment and binding in this process. With that objective, we tested the effect of reduced levels of zDHHC21 on pMLKL levels during necroptosis. We induced necroptosis in shzDHHC21 and shRFP cells and investigated pMLKL levels in these systems using Western blotting. To account any changes in basal expression of MLKL due to zDHHC21 knockdown, we quantified pMLKL levels relative to the total MLKL level. We observed ~50% decrease ($p < 0.01$, t-test) in total pMLKL present in the lysate (**Figure 4A**) and 53% (decrease $p < 0.001$, t-test) in the membrane-localized pMLKL (**Figure 4B**) in shzDHHC21 cells as compared to the control shRFP cells during necroptosis. While the reduction of plasma membrane residing pMLKL is expected upon disruption of its acylation, the overall decrease of pMLKL under these conditions is interesting and suggest that zDHHC21 activity is important for maintaining cellular levels of pMLKL during necroptosis and that reducing zDHHC21 activity decreases cellular pMLKL levels.

Several studies support the role of MLKL and pMLKL in endocytosis, cellular trafficking and exocytosis, processes that not only regulate MLKL homeostasis but also serve to limit the extent of necroptosis. MLKL has been shown to facilitate endocytosis by associating with the endosomal membranes. These endosomes bud into vesicles which fuse with plasma membranes to release MLKL via exocytosis (Yoon et al., 2017). Another study had similar findings showing pMLKL removal from the plasma membrane by exocytosis, thereby protecting cells against membrane rupture and necroptotic cell death (Fan et al., 2019). Based on these previous studies

along with the fact that shzDHHC21 cells exhibited an improved membrane integrity during necroptosis (**Figure 4F**), we decided to probe the extracellular pMLKL levels in these cells to evaluate whether knockdown of zDHHC21 affects release of MLKL to restore membrane integrity. We collected cell culture media from necroptotic and control shzDHHC21 and shRFP cells and isolated the extracellular vesicles by ultracentrifugation. While necroptotic shzDHHC21 cells showed a 33% ($p<0.001$) reduction in pMLKL, released through extracellular vesicles as compared to as shRFP necroptotic cells (**Figure S3A**), the levels of released flotillin 1, a protein commonly associated with extracellular vesicles (Meister and Tikkanen, 2014), also decreased in necroptotic shzDHHC21 cells (18%, $p < 0.01$, **Figure S3B**). These results indicate that there is an overall reduction in extracellular components released in shzDHHC21 cells and that relative pMLKL levels remain unchanged during necroptosis (**Figure 4D**). Altogether, these findings clearly suggest that zDHHC21 activity plays a role in regulating pMLKL levels and maintaining the integrity of the plasma membrane during necroptosis.

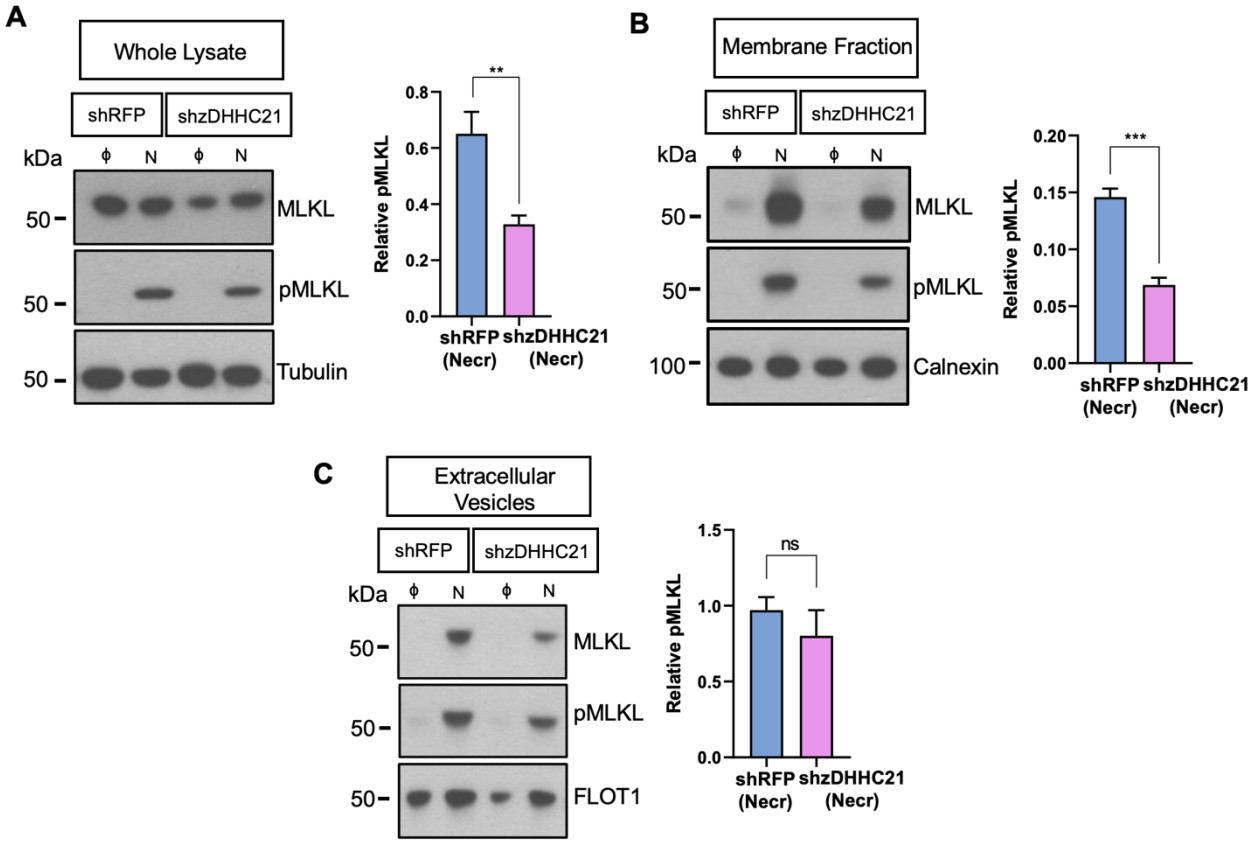

Figure 4: zDHHC21 regulates pMLKL levels during necroptosis. (A) shzDHHC21 has decreased levels of pMLKL present in the cells during necroptosis. Control and necroptotic shRFP and shzDHHC21 whole lysates were normalized based on protein amounts. The samples were blotted for MLKL and pMLKL. Tubulin was used as the loading control. The bar plot represents the quantification for the Western blot. The relative pMLKL to total MLKL levels were calculated

by dividing the corrected intensities of pMLKL (normalized to tubulin) with respective normalized MLKL. Normalized MLKL for shRFP and shzDHHC21 was calculated by dividing the corrected intensities of MLKL (normalized to tubulin) with the average corrected MLKL band intensities in shRFP or shzDHHC21 control. Data represent mean ± 1 SD; n=3. ** represents $p < 0.01$ **(B)** shzDHHC21 cells have decreased pMLKL present at the membrane during necroptosis. Control and necroptotic shRFP and shzDHHC21 cells were fractionated and normalized based on protein amounts. The samples were blotted for MLKL and pMLKL. Calnexin was used as the loading control. The bar plot represents the quantification for the Western blot. The relative pMLKL to total MLKL levels were calculated by dividing the corrected intensities of pMLKL (normalized to calnexin) with respective normalized MLKL. Normalized MLKL for shRFP and shzDHHC21 was calculated by dividing the corrected intensities of MLKL (normalized to calnexin) with the average corrected MLKL band intensities in shRFP or shzDHHC21 control. Data represent mean ± 1 SD; n=3. *** represents $p < 0.001$. **(C)** Levels of pMLKL released from shzDHHC21 and shRFP cells remain unchanged during necroptosis. The bar plot represents relative pMLKL levels released by necroptotic shzDHHC21 and shRFP cells. Media from control and necroptotic shRFP and shzDHHC21 cells was collected, filtered and subjected to ultracentrifugation to collect the extracellular vesicles and exosomes. The samples were normalized based on protein amounts and samples blotted for pMLKL and FLOT1. Dot plot represents relative protein levels calculated by normalizing the corrected intensities for pMLKL with the corrected intensities for FLOT1. Data represent mean ± 1 SD; n=3.

Reducing zDHHC21 activity increased pMLKL degradation. Necroptosis involves a complex and dynamic regulation of MLKL levels. Maintaining a low level of intracellular pMLKL has been suggested as a mechanism to limit necroptotic cell death (Yoon et al., 2017). Another study has shown that pMLKL can be degraded in the lysosomes and that possibly requires the association of pMLKL with the plasma membrane (Fan et al., 2019). Evidence of MLKL being ubiquitylated and being trafficked to endosomes for an eventual release in extracellular vesicles has also been shown (Yoon et al., 2022). Recent studies suggest that ubiquitylated MLKL can be degraded in the proteasome (Hildebrand et al., 2020; Liu et al., 2021) and this degradation of MLKL limits necroptotic cell death. Our results show that reducing zDHHC21 activity during necroptosis decreased pMLKL in cells as well as decreased the extrusion of pMLKL via the extracellular vesicles, leading us to suspect the involvement of degradation pathways and that might impact pMLKL levels when their membrane association is reduced.

We first investigated the link between pMLKL acylation and degradation in necroptosis to understand the reduction in pMLKL levels in shzDHHC21 cells. We treated shRFP and shzDHHC21 cells with (*R*)-MG132, a small molecular inhibitor of the chymotrypsin-like activity of the proteasome (Kisselev and Goldberg, 2001; Lee and Goldberg, 1998). Following treatment with (*R*)-MG132 and induction of necroptosis as we described earlier, cells were collected, subjected to fractionation to collect cytosolic components and analyzed using Western blotting

(**Figure 5A-B**). We compared the effect of (*R*)-MG132 on pMLKL levels in necroptotic shzDHHC21 and necroptotic shRFP cells to assess the contribution of proteasomal degradation in pMLKL levels when its membrane association in reduced. We observed a 43% increase ($p < 0.05$) in pMLKL levels in necroptotic shzDHHC21 cells as compared to necroptotic shRFP cells (**Figure 5B**). These results suggest that the proteasomal degradation of pMLKL is more profound when its acylation is inhibited and that reduced membrane association targets pMLKL for degradation. To validate our observations on reduced acylation promoting pMLKL degradation, we used cycloheximide (CHX) which blocks protein translation (Schneider-Poetsch et al., 2010). Short-term treatment of cells with CHX prevents synthesis of proteins, hence CHX can be a useful tool to study if decreased protein levels are due to increased degradation (Dai et al., 2013). shzDHHC21 and shRFP cells were treated with CHX prior to induction of necroptosis and samples were collected at 0, 3 and 5 hours of necroptosis (**Figure 5C-D**). The effect of zDHHC21 on the degradation of pMLKL in necroptosis is shown by comparing the band intensities of the proteins in shRFP and shzDHHC21 cells in the presence of CHX treatment for 3 and 5 hours of necroptosis, respectively (**Figure 5C**). We observed a 41% and 42% decrease in pMLKL in shzDHHC21 cells treated with CHX after 3 hours and 5 hours of necroptosis respectively ($p < 0.001$ for 3h and $p < 0.05$ for 5h, **Figure 5D**) supporting our observation that reduced acylation of pMLKL increases its degradation. The unchanged levels of MLKL is likely due its longer half-life (determined to be 28h in HeLa cells after CHX treatment) in cells (Zhao et al., 2016). Altogether, these results suggest a mechanism by which zDHHC21-mediated acylation contributes to the retention of MLKL and pMLKL at the plasma membrane during necroptosis, thereby exacerbating membrane permeabilization. By reducing the acylation of pMLKL, the retention of pMLKL at the membrane decreases as well and that targets pMLKL for degradation, leading to an ameliorated necroptotic cell death phenotype (**Figure 5E**).

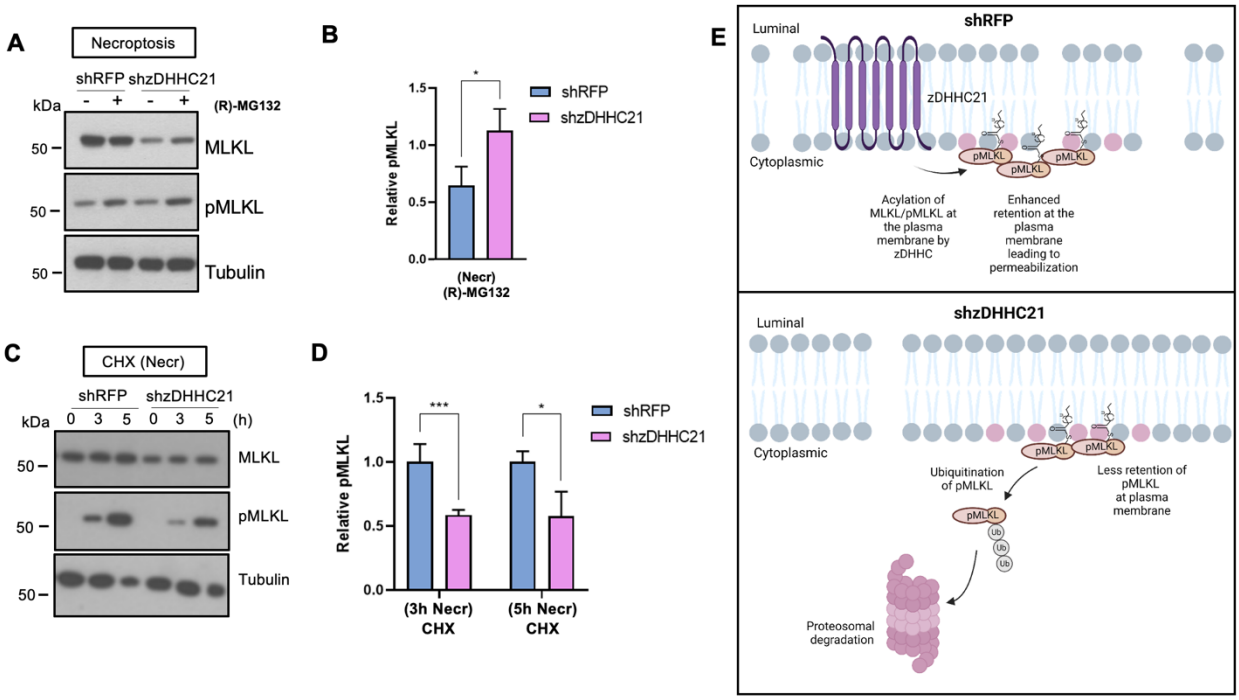

Figure 5. zDHHC21-mediated acylation regulates pMLKL stability during necroptosis. (A) Western blot of cytosolic fraction of shzDHHC21 and shRFP cells after (R)-MG132 treatment. Cells were pretreated with 10 μM (R)-MG132 for 24h, followed by 3h of necroptosis. Cells were fractionated to obtain the cytosolic proteins. Samples were blotted for MLKL and pMLKL. Tubulin was used as a loading control. **(B)** Relative pMLKL levels calculated by dividing the corrected intensities of pMLKL (normalized to tubulin) with respective normalized MLKL. Normalized MLKL for shRFP and shzDHHC21 was calculated by dividing the corrected intensities of MLKL (normalized to tubulin) with the average corrected MLKL band intensities in shRFP or shzDHHC21 control. Data represent mean ± 1 SD; $n = 3$. * represents $p < 0.05$. **(C)** Western blot analysis of shRFP and shzDHHC21 in the presence of 300 μg/mL cycloheximide (CHX). Samples were collected at 0, 3 and 5 h post-necroptosis induction and prepared for Western blotting. Samples were blotted with MLKL, pMLKL and tubulin. **(D)** Quantification of pMLKL in shzDHHC21 relative to shRFP at 3 and 5 h post-necroptosis. The relative intensities are calculated by dividing the corrected intensities of each protein with the corrected intensities of tubulin and normalizing to necroptotic shRFP control. Data represent the mean error bars represent ± 1 SD; n=3. * represents $p < 0.05$, *** represents $p < 0.001$. **(E)** A proposed model for the role of zDHHC21 during necroptosis. Cells promote degradation of pMLKL in necroptosis as a way to limit cell death before being overcome with death signal. Loss of zDHHC21 results in lesser retention of pMLKL at the plasma membranes due to reduced acylation, instead targeting pMLKL for degradation resulting in cell death rescue.

DISCUSSION

Studies on MLKL has gained traction in the past few years (Murphy, 2020). Other than its necroptotic function, not much is known about the physiological role of MLKL, although its

involvement in endocytic trafficking has been recently reported (Yoon et al., 2017). It has been shown that MLKL is maintained in the cytoplasm, which then clusters at the plasma membrane under necroptotic stimuli, leading to membrane disruption. (Samson et al., 2020). In the context of necroptosis, many studies have focused on the pore-forming ability of MLKL; however, the exact mechanisms of its membrane binding by which it induces membrane permeabilization are not completely understood (Flores-Romero et al., 2020).

Previous studies have highlighted the electrostatic interactions between MLKL and the plasma membrane-associated PIP_2 to be an important contributor to membrane binding of MLKL during necroptosis. Adding to these known interactions, we have previously demonstrated that MLKL is acylated during necroptosis. Simulation of a non-acylated MLKL monomer with a membrane model showed PIPs are indeed recruited to the protein binding site (Ramirez et al., 2023). These results support the dynamic interaction between MLKL and membrane lipids and suggest local membrane lipid reorganization upon MLKL binding. In this study, we initially characterized the acylation of several cysteine residues present in each of the regions of MLKL. While the monoacylation MLKL is the predominant form and multiple acylations on the same protein has not been detected, our results show that C184, C269 and C289 can undergo acylation, albeit one at a time, suggesting a promiscuity exists for the cysteine preferences. MD simulations of an acylated monomer at C286 show a particular lipid signature upon interaction with the protein (**Figure 2D**), supporting the acyl chain can cause re-structuring of the membrane lipids and contribute to membrane disruption. We previously discussed the lipid signature in detail for the non-acylated version of the protein (Ramirez et al., 2023); comparing the bound conformations of the protein among the systems listed in Table S1, we observe a conserved lipid fingerprint for the individual conformations, for example, PIP and cholesterol recruitment when the 4HB is bound to the membrane.

We also elaborate on the role of multiple zDHHC members present at the plasma membrane in protein acylation in necroptosis as well as the potential consequences of this acylation in necroptosis. We showed that zDHHC21 has a significant effect on cell membrane integrity and mediating protein acylation in necroptosis. We show that zDHHC21 has a role in regulating pMLKL levels during necroptosis. Reducing the activity of zDHHC21 decreases the membrane association of pMLKL and restores membrane integrity during necroptosis. Further, blocking zDHHC21-mediated pMLKL acylation promoted the degradation of pMLKL, reducing the level of this key signaling protein.

Based on these results and our previous findings (Pradhan et al., 2021), we envision a dual role for pMLKL acylation in necroptosis. First, this acylation is important for pMLKL function during necroptosis as it increases membrane binding and contributes to membrane permeabilization during necroptosis. Second, acylation of pMLKL specifically by VLCFAs contributes to membrane disruption, mediated by lipid reorganization induced by VLCFA insertion to the plasma membrane (**Figure 2** and **Table S1**). Studies to dissect the mechanisms that govern and prefer acylation by VLCFAs compared to common palmitoylation are warranted. Overall, these results establish previously unknown mechanisms that modulate pMLKL functioning during necroptosis and suggest that inhibition of pMLKL acylation can be a strategy to reduce membrane permeabilization during necroptosis.

EXPERIMENTAL PROCEDURES

Detailed information on the materials used can be found in the Supplemental Experimental Procedures section, as well as detailed procedures for cell culture and other analyses.

SUPPLEMENTAL INFORMATION

Supplemental Information includes 3 figures and 3 tables, materials used, experimental procedures and can be found with this article online.

ACKNOWLEDGMENTS

We acknowledge the support from the National Science Foundation grant (MCB1817468 to G.E.A.G.) and The Research Foundation, The State University of New York (#1181362). Simulations were run in part at the University at Buffalo's Center for Computational Research (Center for Computational Research, 2019) and in the Anton2 machine. Anton2 computer time was provided by the Pittsburgh Supercomputing Center (PSC) through Grant R01GM116961 from the National Institutes of Health, specific award MCB200093P. The Anton2 machine as PSC was generously made available by D.E. Shaw Research (Shaw et al., 2014).

AUTHOR CONTRIBUTIONS

Experiments were designed by A.J.P., V. M-G., Y.S. and G.E.A-G. The experiments were conducted by A.J.P., S.C.Y.S. The all-atom molecular dynamic simulations were conducted by R.X.R. and V.M-G. The manuscript was written by A.J.P., R.X.R., V. M-G. and G.E.A-G. The study was directed by G.E.A-G. The authors declare no conflict of interest.

REFERENCES

Abraham, M. J., Murtola, T., Schulz, R., Páll, S., Smith, J. C., Hess, B. & Lindahl, E. (2015). GROMACS: High performance molecular simulations through multi-level parallelism from laptops to supercomputers. SoftwareX, *1-2,* 19-25.

Beard, R. S., Yang, X., Meegan, J. E., Overstreet, J. W., Yang, C. G. Y., Elliott, J. A., Reynolds, J. J., Cha, B. J., Pivetti, C. D., Mitchell, D. A., Wu, M. H., Deschenes, R. J. & Yuan, S. Y. (2016). Palmitoyl acyltransferase DHHC21 mediates endothelial dysfunction in systemic inflammatory response syndrome. Nat. Commun. *7*, 12823.

Blanc, M., David, F., Abrami, L., Migliozzi, D., Armand, F., Bürgi, J. & Van Der Goot, F. G. (2015). SwissPalm: Protein Palmitoylation database. F1000Res*. 4,* 261.

Blanc, M., David, F. P. A. & Van Der Goot, F. G. (2019). SwissPalm 2: Protein S-Palmitoylation Database. Methods Mol. Biol. *2009*, 203-214.

Center for Computational Research, U. a. B. (2019).
[Available at: https://ubir.buffalo.edu/xmlui/handle/10477/79221.]

Chen, X., Li, W., Ren, J., Huang, D., He, W. T., Song, Y., Yang, C., Li, W., Zheng, X., Chen, P. & Han, J. (2014). Translocation of mixed lineage kinase domain-like protein to plasma membrane leads to necrotic cell death. Cell Res*. 24*, 105-121.

Dai, C. L., Shi, J., Chen, Y., Iqbal, K., Liu, F. & Gong, C. X. (2013). Inhibition of protein synthesis alters protein degradation through activation of protein kinase B (AKT). J. Biol. Chem. *288*, 23875-23883.

Darden, T., York, D. & Pedersen, L. (1993). Particle mesh Ewald: An N·log(N) method for Ewald sums in large systems. J. Chem. Phys. *98,* 10089-10092.

Davies, K. A., Tanzer, M. C., Griffin, M. D. W., Mok, Y. F., Young, S. N., Qin, R., Petrie, E. J., Czabotar, P. E., Silke, J. & Murphy, J. M. (2018). The brace helices of MLKL mediate interdomain communication and oligomerisation to regulate cell death by necroptosis. Cell Death Differ. *25*, 1567-1580.

Dondelinger, Y., Declercq, W., Montessuit, S., Roelandt, R., Goncalves, A., Bruggeman, I., Hulpiau, P., Weber, K., Sehon, C. A., Marquis, R. W., Bertin, J., Gough, P. J., Savvides, S., Martinou, J. C., Bertrand, M. J. & Vandenabeele, P. (2014). MLKL compromises plasma membrane integrity by binding to phosphatidylinositol phosphates. Cell Rep. *7*, 971-981.

Fan, W., Guo, J., Gao, B., Zhang, W., Ling, L., Xu, T., Pan, C., Li, L., Chen, S., Wang, H., Zhang, J. & Wang, X. (2019). Flotillin-mediated endocytosis and ALIX–syntenin-1–mediated exocytosis protect the cell membrane from damage caused by necroptosis. Sci. Signal. 12, eaaw3423.

Flores-Romero, H., Ros, U. & Garcia-Saez, A. J. (2020). Pore formation in regulated cell death. EMBO J. *39*, e105753.

Gibellini, L. & Moro, L. (2021). Programmed Cell Death in Health and Disease. *Cells,* 10.

Gottlieb, C. D., Zhang, S. & Linder, M. E. 2015. The Cysteine-rich Domain of the DHHC3 Palmitoyltransferase Is Palmitoylated and Contains Tightly Bound Zinc*. J. Biol. Chem. *290*, 29259-29269.

Gough, P. & Myles, I. A. (2020). Tumor Necrosis Factor Receptors: Pleiotropic Signaling Complexes and Their Differential Effects. Front. Immunol. 11.

Greaves, J., Munro, K. R., Davidson, S. C., Riviere, M., Wojno, J., Smith, T. K., Tomkinson, N. C. & Chamberlain, L. H. (2017). Molecular basis of fatty acid selectivity in the zDHHC family of S-acyltransferases revealed by click chemistry. Proc. Natl. Acad. Sci. U. S. A*. 114*, E1365-e1374.

Green, D. R. (2022). Cell Death in Development. Cold Spring Harb. Perspect. Biol. 14.

Guillou, H., Zadravec, D., Martin, P. G. P. & Jacobsson, A. (2010). The key roles of elongases and desaturases in mammalian fatty acid metabolism: Insights from transgenic mice. Prog. Lipid Res. *49*, 186-199.

He, M., Abdi, K. M. & Bennett, V. (2014). Ankyrin-G palmitoylation and βII-spectrin binding to phosphoinositide lipids drive lateral membrane assembly. *J Cell Biol,* 206**,** 273-88.

Hildebrand, J. M., Kauppi, M., Majewski, I. J., Liu, Z., Cox, A. J., Miyake, S., Petrie, E. J., Silk, M. A., Li, Z., Tanzer, M. C., Brumatti, G., Young, S. N., Hall, C., Garnish, S. E., Corbin, J., Stutz, M. D., Di Rago, L., Gangatirkar, P., Josefsson, E. C., Rigbye, K., Anderton, H., Rickard, J. A., Tripaydonis, A., Sheridan, J., Scerri, T. S., Jackson, V. E., Czabotar, P. E., Zhang, J.-G., Varghese, L., Allison, C. C., Pellegrini, M., Tannahill, G. M., Hatchell, E. C., Willson, T. A., Stockwell, D., De Graaf, C. A., Collinge, J., Hilton, A., Silke, N., Spall, S. K., Chau, D., Athanasopoulos, V., Metcalf, D., Laxer, R. M., Bassuk, A. G., Darbro, B. W., Fiatarone Singh, M. A., Vlahovich, N., Hughes, D., Kozlovskaia, M., Ascher, D. B., Warnatz, K., Venhoff, N., Thiel, J., Biben, C., Blum, S., Reveille, J., Hildebrand, M. S., Vinuesa, C. G., Mccombe, P., Brown, M. A., Kile, B. T., Mclean, C., Bahlo, M., Masters, S. L., Nakano, H., Ferguson, P. J., Murphy, J. M., Alexander, W. S. & Silke, J. (2020). A missense mutation in the MLKL brace region promotes lethal neonatal inflammation and hematopoietic dysfunction. Nat. Commun. *11*, 3150.

Hildebrand, J. M., Tanzer, M. C., Lucet, I. S., Young, S. N., Spall, S. K., Sharma, P., Pierotti, C., Garnier, J.-M., Dobson, R. C. J., Webb, A. I., Tripaydonis, A., Babon, J. J., Mulcair, M. D., Scanlon, M. J., Alexander, W. S., Wilks, A. F., Czabotar, P. E., Lessene, G., Murphy, J. M. & Silke, J. (2014). Activation of the pseudokinase MLKL unleashes the four-helix bundle domain to induce membrane localization and necroptotic cell death. Proc. Natl. Acad. Sci. U. S. A. *111*, 15072-15077.

Hilgemann, D. W., Fine, M., Linder, M. E., Jennings, B. C. & Lin, M. J. (2013). Massive endocytosis triggered by surface membrane palmitoylation under mitochondrial control in BHK fibroblasts. Elife. *2,* e01293.

Huang, D., Zheng, X., Wang, Z. A., Chen, X., He, W. T., Zhang, Y., Xu, J. G., Zhao, H., Shi, W., Wang, X., Zhu, Y. & Han, J. (2017a). The MLKL Channel in Necroptosis Is an Octamer Formed by Tetramers in a Dyadic Process. Mol. Cell. Biol. *37*, e00497-16.

Huang, J., Rauscher, S., Nawrocki, G., Ran, T., Feig, M., De Groot, B. L., Grubmüller, H. & Mackerell, A. D., Jr. (2017b). CHARMM36m: an improved force field for folded and intrinsically disordered proteins. Nat. Methods. *14*, 71-73.

Jennings, B. C. & Linder, M. E. (2012). DHHC Protein S-Acyltransferases Use Similar Ping-Pong Kinetic Mechanisms but Display Different Acyl-CoA Specificities*. J. Biol. Chem. *287*, 7236-7245.

Jiang, H., Zhang, X., Chen, X., Aramsangtienchai, P., Tong, Z. & Lin, H. (2018). Protein Lipidation: Occurrence, Mechanisms, Biological Functions, and Enabling Technologies. Chem. Rev. *118*, 919-988.

Jo, S., Lim, J. B., Klauda, J. B. & Im, W. (2009). CHARMM-GUI Membrane Builder for mixed bilayers and its application to yeast membranes. Biophys. J. *97*, 50-68.

Kaczmarek, A., Vandenabeele, P. & Krysko, D. V. (2013). Necroptosis: the release of damage-associated molecular patterns and its physiological relevance. Immunity. *38*, 209-223.

Kisselev, A. F. & Goldberg, A. L. (2001). Proteasome inhibitors: from research tools to drug candidates. Chem. Biol. *8,* 739-758.

Klauda, J. B., Venable, R. M., Freites, J. A., O'connor, J. W., Tobias, D. J., Mondragon-Ramirez, C., Vorobyov, I., Mackerell, A. D., Jr. & Pastor, R. W. (2010). Update of the CHARMM All-Atom Additive Force Field for Lipids: Validation on Six Lipid Types. J. Phys. Chem. B. *114*, 7830-7843.

Lee, D. H. & Goldberg, A. L. (1998). Proteasome inhibitors: valuable new tools for cell biologists. Trends Cell Biol. *8*, 397-403.

Lee, J., Patel, D. S., Ståhle, J., Park, S. J., Kern, N. R., Kim, S., Lee, J., Cheng, X., Valvano, M. A., Holst, O., Knirel, Y. A., Qi, Y., Jo, S., Klauda, J. B., Widmalm, G. & Im, W. (2019). CHARMM-GUI Membrane Builder for Complex Biological Membrane Simulations with Glycolipids and Lipoglycans. J. Chem. Theory Comput. *15*, 775-786.

Liu, S., Liu, H., Johnston, A., Hanna-Addams, S., Reynoso, E., Xiang, Y. & Wang, Z. (2017). MLKL forms disulfide bond-dependent amyloid-like polymers to induce necroptosis. Proc. Natl. Acad. Sci. U. S. A. *114*, E7450.

Liu, Z., Dagley, L. F., Shield-Artin, K., Young, S. N., Bankovacki, A., Wang, X., Tang, M., Howitt, J., Stafford, C. A., Nachbur, U., Fitzgibbon, C., Garnish, S. E., Webb, A. I., Komander, D., Murphy, J. M., Hildebrand, J. M. & Silke, J. (2021). Oligomerization-driven MLKL ubiquitylation antagonizes necroptosis. EMBO J. *40*, e103718.
Lu, D., Parisi, L. R., Gokcumen, O. & Atilla-Gokcumen, G. E. (2023). SREBP activation contributes to fatty acid accumulations in necroptosis. RSC Chem. Biol. *4*, 310-322.
Meister, M. & Tikkanen, R. (2014). Endocytic Trafficking of Membrane-Bound Cargo: A Flotillin Point of View. Membranes. *4*, 356-371.
Molnár, T., Mázló, A., Tslaf, V., Szöllősi, A. G., Emri, G. & Koncz, G. (2019). Current translational potential and underlying molecular mechanisms of necroptosis. Cell Death Dis. *10*, 860.
Murphy, J. M. (2020). The Killer Pseudokinase Mixed Lineage Kinase Domain-Like Protein (MLKL). Cold Spring Harb. Perspect. Biol. 12, a036376.
Murphy, J. M., Czabotar, P. E., Hildebrand, J. M., Lucet, I. S., Zhang, J. G., Alvarez-Diaz, S., Lewis, R., Lalaoui, N., Metcalf, D., Webb, A. I., Young, S. N., Varghese, L. N., Tannahill, G. M., Hatchell, E. C., Majewski, I. J., Okamoto, T., Dobson, R. C., Hilton, D. J., Babon, J. J., Nicola, N. A., Strasser, A., Silke, J. & Alexander, W. S. (2013). The pseudokinase MLKL mediates necroptosis via a molecular switch mechanism. Immunity. *39*, 443-53.
Ohno, Y., Kihara, A., Sano, T. & Igarashi, Y. (2006). Intracellular localization and tissue-specific distribution of human and yeast DHHC cysteine-rich domain-containing proteins. Biochim. Biophys. Acta. *1761*, 474-483.
Parisi, L. R., Li, N. & Atilla-Gokcumen, G. E. (2017). Very Long Chain Fatty Acids Are Functionally Involved in Necroptosis. Cell Chem. Biol. *24*, 1445-1454.e8.
Parisi, L. R., Sowlati-Hashjin, S., Berhane, I. A., Galster, S. L., Carter, K. A., Lovell, J. F., Chemler, S. R., Karttunen, M. & Atilla-Gokcumen, G. E. (2019). Membrane Disruption by Very Long Chain Fatty Acids during Necroptosis. ACS Chem. Biol. *14*, 2286-2294.
Parrinello, M. & Rahman, A. (1981). Polymorphic transitions in single crystals: A new molecular dynamics method. J. Appl. Phys. *52*, 7182-7190.
Percher, A., Thinon, E. & Hang, H. (2017). Mass-Tag Labeling Using Acyl-PEG Exchange for the Determination of Endogenous Protein S-Fatty Acylation. Curr. Protoc. Protein Sci. *89*, 14 17 1-14 17 11.
Petrie, E. J., Birkinshaw, R. W., Koide, A., Denbaum, E., Hildebrand, J. M., Garnish, S. E., Davies, K. A., Sandow, J. J., Samson, A. L., Gavin, X., Fitzgibbon, C., Young, S. N., Hennessy, P. J., Smith, P. P. C., Webb, A. I., Czabotar, P. E., Koide, S. & Murphy, J. M. (2020). Identification of MLKL membrane translocation as a checkpoint in necroptotic cell death using Monobodies. Proc. Natl. Acad. Sci. U. S. A. *117*, 8468.
Petrie, E. J., Sandow, J. J., Jacobsen, A. V., Smith, B. J., Griffin, M. D. W., Lucet, I. S., Dai, W., Young, S. N., Tanzer, M. C., Wardak, A., Liang, L.-Y., Cowan, A. D., Hildebrand, J. M., Kersten, W. J. A., Lessene, G., Silke, J., Czabotar, P. E., Webb, A. I. & Murphy, J. M (2018). Conformational switching of the pseudokinase domain promotes human MLKL tetramerization and cell death by necroptosis. Nat. Commun. *9*, 2422.
Plain, F., Congreve, S. D., Yee, R. S. Z., Kennedy, J., Howie, J., Kuo, C. W., Fraser, N. J. & Fuller, W. (2017). An amphipathic α-helix directs palmitoylation of the large intracellular loop of the sodium/calcium exchanger. J. Biol. Chem. *292*, 10745-10752.
Plain, F., Howie, J., Kennedy, J., Brown, E., Shattock, M. J., Fraser, N. J. & Fuller, W. (2020). Control of protein palmitoylation by regulating substrate recruitment to a zDHHC-protein acyltransferase. Commun. Biol. *3*, 411.
Pradhan, A. J., Lu, D., Parisi, L. R., Shen, S., Berhane, I. A., Galster, S. L., Bynum, K., Monje-Galvan, V., Gokcumen, O., Chemler, S. R., Qu, J., Kay, J. G. & Atilla-Gokcumen, G. E. (2021). Protein acylation by saturated very long chain fatty acids and endocytosis are involved in necroptosis. Cell Chem. Biol. *28*, 1298-1309.e7.

Quarato, G., Guy, C. S., Grace, C. R., Llambi, F., Nourse, A., Rodriguez, D. A., Wakefield, R., Frase, S., Moldoveanu, T. & Green, D. R. (2016). Sequential Engagement of Distinct MLKL Phosphatidylinositol-Binding Sites Executes Necroptosis. Mol. Cell. *61*, 589-601.
Ramirez, R. X., Campbell, O., Pradhan, A. J., Atilla-Gokcumen, G. E. & Monje-Galvan, V. (2023). Modeling the molecular fingerprint of protein-lipid interactions of MLKL on complex bilayers. Front. Chem. 10, 1088058.
Rana, M. S., Kumar, P., Lee, C.-J., Verardi, R., Rajashankar, K. R. & Banerjee, A. (2018). Fatty acyl recognition and transfer by an integral membrane *S*-acyltransferase. Science. *359*, eaao6326.
Samson, A. L., Zhang, Y., Geoghegan, N. D., Gavin, X. J., Davies, K. A., Mlodzianoski, M. J., Whitehead, L. W., Frank, D., Garnish, S. E., Fitzgibbon, C., Hempel, A., Young, S. N., Jacobsen, A. V., Cawthorne, W., Petrie, E. J., Faux, M. C., Shield-Artin, K., Lalaoui, N., Hildebrand, J. M., Silke, J., Rogers, K. L., Lessene, G., Hawkins, E. D. & Murphy, J. M. (2020). MLKL trafficking and accumulation at the plasma membrane control the kinetics and threshold for necroptosis. Nat. Commun. *11*, 3151.
Schneider-Poetsch, T., Ju, J., Eyler, D. E., Dang, Y., Bhat, S., Merrick, W. C., Green, R., Shen, B. & Liu, J. O. (2010). Inhibition of eukaryotic translation elongation by cycloheximide and lactimidomycin. Nat. Chem. Biol. *6*, 209-217.
Sethi, A., Horne, C. R., Fitzgibbon, C., Wilde, K., Davies, K. A., Garnish, S. E., Jacobsen, A. V., Samson, A. L., Hildebrand, J. M., Wardak, A., Czabotar, P. E., Petrie, E. J., Gooley, P. R. & Murphy, J. M. (2022). Membrane permeabilization is mediated by distinct epitopes in mouse and human orthologs of the necroptosis effector, MLKL. Cell Death Differ. *29*, 1804-1815.
Shaw, D. E., Grossman, J. P., Bank, J. A., Batson, B., Butts, J. A., Chao, J. C., Deneroff, M. M., Dror, R. O., Even, A., Fenton, C. H., Forte, A., Gagliardo, J., Gill, G., Greskamp, B., Ho, C. R., Ierardi, D. J., Iserovich, L., Kuskin, J. S., Larson, R. H., Layman, T., Lee, L. S., Lerer, A. K., Li, C., Killebrew, D., Mackenzie, K. M., Mok, S. Y. H., Moraes, M. A., Mueller, R., Nociolo, L. J., Peticolas, J. L., Quan, T., Ramot, D., Salmon, J. K., Scarpazza, D. P., Schafer, U. B., Siddique, N., Snyder, C. W., Spengler, J., Tang, P. T. P., Theobald, M., Toma, H., Towles, B., Vitale, B., Wang, S. C. & Young, C. Anton 2: Raising the Bar for Performance and Programmability in a Special-Purpose Molecular Dynamics Supercomputer. SC '14: Proceedings of the International Conference for High Performance Computing, Networking, Storage and Analysis, 16-21 Nov. 2014 (2014). 41-53.
Stewart, S. A., Dykxhoorn, D. M., Palliser, D., Mizuno, H., Yu, E. Y., An, D. S., Sabatini, D. M., Chen, I. S., Hahn, W. C., Sharp, P. A., Weinberg, R. A. & Novina, C. D. (2003). Lentivirus-delivered stable gene silencing by RNAi in primary cells. RNA. *9*, 493-501.
Su, L., Quade, B., Wang, H., Sun, L., Wang, X. & Rizo, J. (2014). A plug release mechanism for membrane permeation by MLKL. Structure. *22*, 1489-500.
Sun, L., Wang, H., Wang, Z., He, S., Chen, S., Liao, D., Wang, L., Yan, J., Liu, W., Lei, X. & Wang, X. (2012). Mixed lineage kinase domain-like protein mediates necrosis signaling downstream of RIP3 kinase. Cell. *148*, 213-227.
Vandenabeele, P., Galluzzi, L., Vanden Berghe, T. & Kroemer, G. (2010). Molecular mechanisms of necroptosis: an ordered cellular explosion. Nat. Rev. Mol. Cell Biol. *11*, 700-714.
Vanommeslaeghe, K. & Mackerell, A. D., Jr. (2012). Automation of the CHARMM General Force Field (CGenFF) I: Bond Perception and Atom Typing. J. Chem. Inf. Model. *52*, 3144-3154.
Wang, H., Sun, L., Su, L., Rizo, J., Liu, L., Wang, L. F., Wang, F. S. & Wang, X. (2014). Mixed lineage kinase domain-like protein MLKL causes necrotic membrane disruption upon phosphorylation by RIP3. Mol. Cell. *54*, 133-146.
Yang, X., Zheng, E., Ma, Y., Chatterjee, V., Villalba, N., Breslin, J. W., Liu, R., Wu, M. H. & Yuan, S. Y. (2021). DHHC21 deficiency attenuates renal dysfunction during septic injury. Sci. Rep. *11*, 11146.

Yoon, S., Bogdanov, K. & Wallach, D. (2022). Site-specific ubiquitination of MLKL targets it to endosomes and targets Listeria and Yersinia to the lysosomes. Cell Death Differ. *29*, 306-322.
Yoon, S., Kovalenko, A., Bogdanov, K. & Wallach, D. (2017). MLKL, the Protein that Mediates Necroptosis, Also Regulates Endosomal Trafficking and Extracellular Vesicle Generation. Immunity. *47*, 51-65.e7.
Zhang, Y., Liu, J., Yu, D., Zhu, X., Liu, X., Liao, J., Li, S. & Wang, H. (2021). The MLKL kinase-like domain dimerization is an indispensable step of mammalian MLKL activation in necroptosis signaling. Cell Death Dis. *12*, 638.
Zhao, X. M., Chen, Z., Zhao, J. B., Zhang, P. P., Pu, Y. F., Jiang, S. H., Hou, J. J., Cui, Y. M., Jia, X. L. & Zhang, S. Q. (2016). Hsp90 modulates the stability of MLKL and is required for TNF-induced necroptosis. Cell Death Dis. *7*, e2089-e2089.

Supplemental Information for

Acylation of MLKL impacts its function in necroptosis

Apoorva Pradhan,[1] Shweta Chitkara,[1] Ricardo X. Ramirez,[2] Viviana Monje-Galvan,[2] Yasemin Sancak,[3] G. Ekin Atilla-Gokcumen[1]*

[1] Department of Chemistry, University at Buffalo, The State University of New York, Buffalo, New York 14260, USA

[2] Department of Chemical and Biological Engineering, University at Buffalo, The State University of New York, Buffalo, New York 14260, USA

[3] Department of Pharmacology, University of Washington, Seattle, Washington 98195, USA

*Corresponding author: ekinatil@buffalo.edu

Figure S1. (A) Overlay of the human and mouse MLKL with the cysteines in human MLKL highlighted in red with residue numbers in boxes above. The corresponding residues for mouse MLKL are marked in green. **(B)** Acyl PEG exchange with N-ethylmaleimide (NEM), hydroxylamine (NH_2OH) and methoxypolyethylene glycol maleimide (mPEG-Mal) was performed on control WT-MLKL and cysteine mutant cells. The conditions without NH_2OH (represented by -) are controls for presence of acylation. The samples are blotted for myc. The control cells (not induced with necroptosis) show no distinguishable acylation/migration.

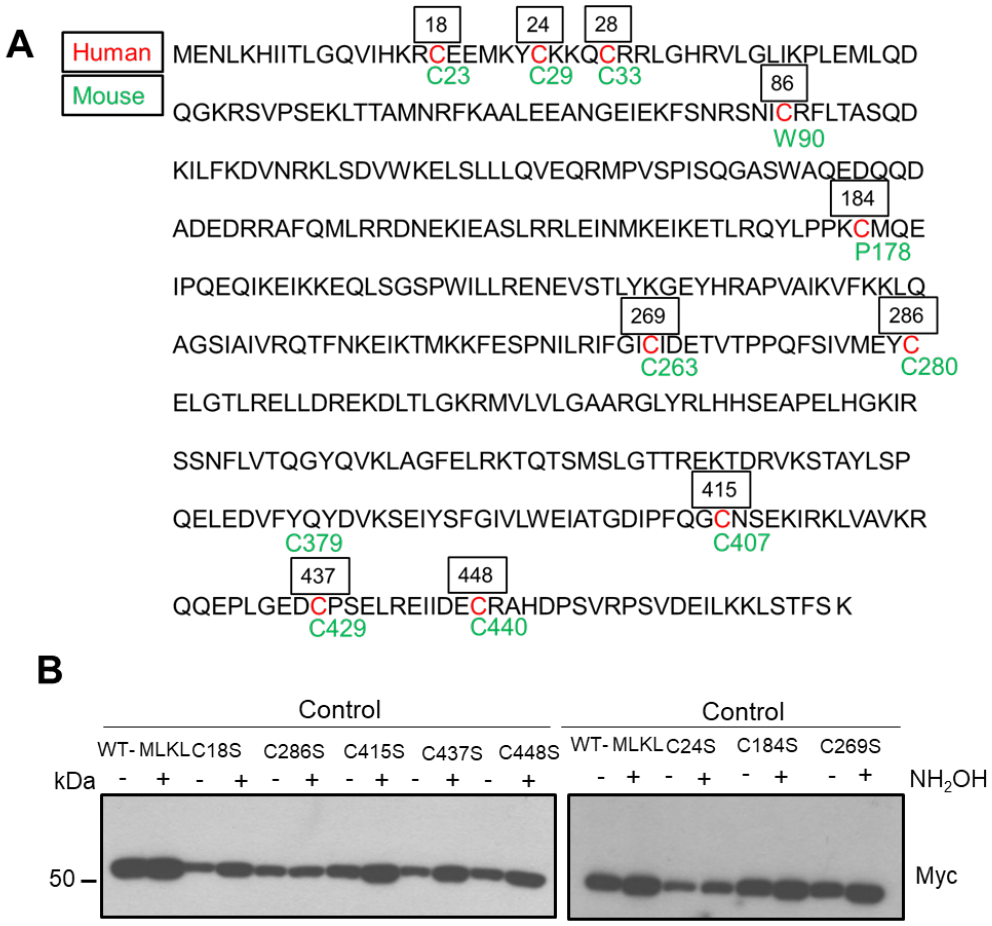

Figure S2. (A) Acyl PEG exchange with NEM, NH_2OH and mPEG-Mal necroptotic shRFP and shzDHHC20 cells. The conditions without NH_2OH (represented by -) are controls for presence of acylation. The samples are blotted for MLKL and pMLKL. **(B)** Quantification of acylated MLKL and pMLKL in shzDHHC20 compared to shRFP. The ratio is calculated by dividing migrated band intensities of pMLKL with non-migrated band intensities. No significant change in the extent of acylation between the two conditions was observed.

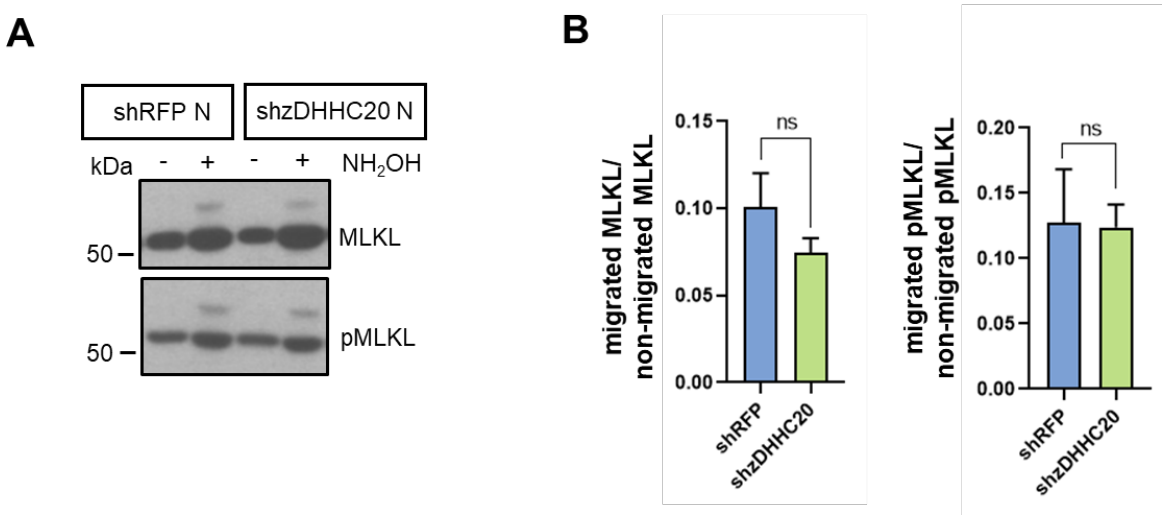

Figure S3. (A) Quantification showing shzDHHC21 has decreased pMLKL released in media in necroptosis. Media from control and necroptotic shRFP and shzDHHC21 cells was collected, filtered and subjected to ultracentrifugation to collect the extracellular vesicles and exosomes. The samples were normalized based on protein amounts and samples blotted for pMLKL. Bar plot represents relative protein levels calculated by normalizing the corrected intensities for each protein with the corresponding values for that protein for shRFP necroptotic condition. Data represent mean ± 1 SD; n=3. ** represents $p < 0.01$. **(B)** Quantification showing shzDHHC21 has decreased protein content released in media in necroptosis. Media from control and necroptotic shRFP and shzDHHC21 cells was collected, filtered and subjected to ultracentrifugation to collect the extracellular vesicles and exosomes. The samples were normalized based on protein amounts and samples blotted for FLOT1. Bar plot represents relative protein levels calculated by normalizing the corrected intensities for each protein with the corresponding values for that protein for shRFP necroptotic condition.

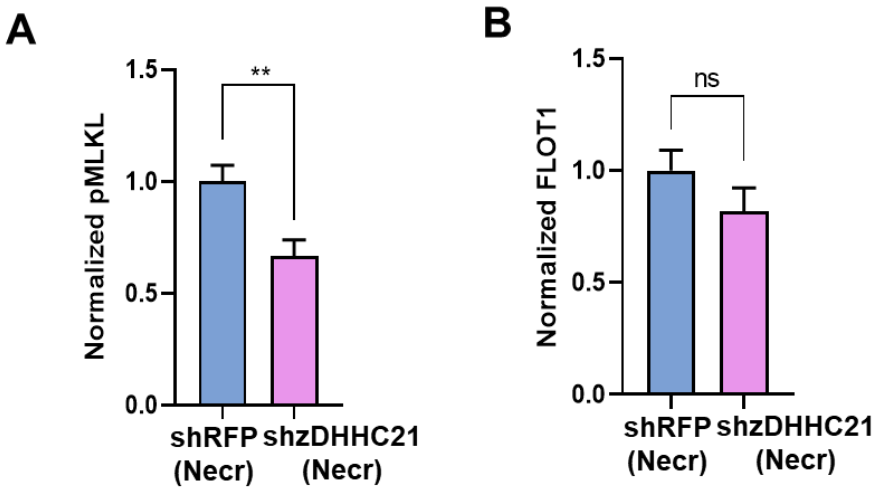

Table S1. **Related to Figure 1.** Cysteine occupancies as percent of time each residue spent interacting with membrane lipids during the simulation. Cysteines of mouse MLKL presented with corresponding human MLKL residues shown in red. The trajectories for replicas 1, 2, 3 and 4 (Rep1, Rep2, Rep3 and Rep4) for the non-acylated MLKL have been previously published in Ramirez *et al*. (Ramirez et al., 2023)

		C23 **C18**	**C29** **C24**	**C33** **C28**	**C174** **L180**	**C263** **C269**	**C280** **C286**	**C379** **Y387**	**C407** **C415**	**C429** **C437**	**C440** **C448**
Non-acylated MLKL	**Rep1**	0.00	0.00	0.00	0.00	18.68	0.44	0.44	**100.00**	0.00	0.00
	Rep2	**31.69**	0.44	10.48	0.00	0.84	0.00	**56.60**	0.79	0.00	0.00
	Rep3	**68.38**	1.83	13.74	0.57	0.00	0.00	0.00	0.00	1.88	0.00
	Rep4	0.00	0.00	0.00	14.78	0.09	**46.14**	0.44	**99.83**	10.03	0.00
Acylated -MLKL	**280r1** **286**	0.95	0.00	0.00	70.63	1.91	86.66	0.00	4.70	0.00	0.00
	280r2 **286**	0.00	0.00	0.00	1.72	5.34	60.17	0.00	83.97	0.10	0.00
	280r3 **286**	0.00	0.00	0.00	23.41	1.15	56.33	0.00	91.94	0.57	0.00

Table S2. Sequences of primers used to introduce point mutations:

Cysteine target	Primer sequence
C18S	Forward: GTCATCCACAAACGGAGTGAAGAGATGAAATAC Reverse: GTATTTCATCTCTTCACTCCGTTTGTGGATGAC
C24S	Forward: GAAGAGATGAAATACAGCAAGAAACAGTGCCGG Reverse: CCGGCACTGTTTCTTGCTGTATTTCATCTCTTC
C184S	Forward: CAGTATTTACCACCAAAAAGCATGCAGGAGATCCCG Reverse: CGGGATCTCCTGCATGCTTTTTGGTGGTAAATACTG
C269S	Forward: CTGCGTATATTTGGGATTAGCATTGATGAAACAGTGACTCCG Reverse: CGGAGTCACTGTTTCATCAATGCTAATCCCAAATATACGCAG
C286S	Forward: ATTGTCATGGAGTACAGTGAACTCGGGACCCTG Reverse: CAGGGTCCCGAGTTCACTGTACTCCATGACAAT
C415S	Forward: ATCCCGTTTCAAGGCAGTAATTCTGAGAAGATC Reverse: GATCTTCTCAGAATTACTGCCTTGAAACGGGAT
C437S	Forward: CCACTGGGTGAAGACAGCCCTTCAGAGCTGCGG Reverse: CCGCAGCTCTGAAGGGCTGTCTTCACCCAGTGG
C448S	Forward: GAGATCATTGATGAGAGCCGGGCCCATGATCCC Reverse: GGGATCATGGGCCCGGCTCTCATCAATGATCTC

Table S3. Sequences of primers used for droplet digital PCR:

Target	Primer and probe sequence
zDHHC5	Forward: CAGGGAAAGGAGGAAAAGGAA Reverse: GTCTGTACAACTGTGTGGAG Probe: 56-FAM/AACTGTATT/ZEN/GGTCGCCGGAACTACC/3IABkFQ
zDHHC20	Forward: CCATTTCCATCAGGTCCGTAT Reverse: GTTCTTCATCAGCGTCCTCTC Probe: 56-FAM/TTCCAACTA/ZEN/GCCAGCAGTGGTAGC/3IABkFQ
zDHHC21	Forward: CACTTGTTACATAATTCCCAGAACT Reverse: GGCCTCCATAACTGATCCAG Probe: 56-FAM/CCTGAGAAC/ZEN/CCCAAGATCCCACAT/3IABkFQ
HPRT1	Forward: GTATTCATTATAGTCAAGGGCATATCC Reverse: AGATGGTCAAGGTCGCAAG Probe: 5HEX/TGGTGAAAA/ZEN/GGACCCCACGAAGT/3IABkFQ/

EXPERIMENTAL MODEL AND SUBJECT DETAILS

Materials and Methods. The cell lines were obtained from ATCC® (HT-29 cells, HTB38, adult Caucasian female origin). For the cell culture, DMEM and penicillin/streptomycin were obtained from Corning, FBS was obtained from Sigma and trypsin (from bovine pancreas) was obtained from Millipore Sigma (Cat. # T6567-5X20UG; CAS: 9002-07-7). Plasmids were obtained from Millipore Sigma (shzDHHC5 andshzDHHC21 in pLKO.1 vectors provided as bacterial glycerol stocks, shzDHHC5: NM_015457, TRCN0000162357; shzDHHC21: NM_178566, TRCN0000144923). Lenti ORF clone of human MLKL from Origene was subcloned into plasmid pLYS1-Myc and sequence verified; psPAX2 was a gift from Dr. Didier Trono (Addgene plasmid, Cat. # 12260); pCMV-VSV-G was a gift from Dr. Bob Weinberg [(Stewart et al., 2003); Addgene plasmid, Cat. # 8854], shRFP (rfp_59s1c1; TRCN0000072205) was a gift by Dr. Yasemin Sancak and shzDHHC20 was a gift by Dr. Eric Witze. The QuikChange II XL Site-Directed Mutagenesis Kit was obtained from Agilent Technologies (Cat. # 200521). For plasmid extraction, the E.Z.N.A® Plasmid DNA Mini Kit was obtained from Omega Bio-Tek (Cat. # D6945-01).

TNF-α (carrier free) was obtained from R&D Systems (Cat. # 210-TA/CF), BV6 was obtained from Selleck Chemicals (Cat. # S7597; CAS: 1001600-56-1) and zVAD-FMK was obtained from Enzo Life Sciences (Cat. # ALX-260-020; CAS: 220644-02-0). Propidium Iodide, Pierce™ Protease Inhibitor (Cat. # A32955), Pierce™ High Capacity Neutravidin Agarose (Cat. # 29202) and M-PER™ Mammalian Protein Extraction Reagent (Cat. # 78501) were obtained from ThermoFisher Scientific. Puromycin (Cat. # P8833; CAS: 58-58-2), Polybrene (Cat. # TR-1003) and X-treme GENE 9 transfection reagent (Cat. # XTG9-RO) were obtained from Millipore Sigma. Cycloheximide (Cat. # 14126) was obtained from Cayman Chemicals.

Antibodies were obtained from Cell Signaling Technology (rabbit monoclonal anti-MLKL, Cat. # 14993S, RRID: AB_2721822; rabbit monoclonal anti-pMLKL, Cat. #91689, RRID: AB_2732034, rabbit monoclonal anti-Myc tag, Cat. #2278, RRID: AB_490778, rabbit monoclonal anti-calnexin, Cat. # 2679S, RRID: AB_2228381), Proteintech (rabbit polyclonal anti-Flotillin 1, Cat. # 15571-1-AP, RRID: AB_2106746), Millipore Sigma (mouse monoclonal anti-α tubulin, Cat. # T9026, RRID: AB_477593), Promega (goat anti-rabbit HRP conjugate, Cat. # W4011, RRID: AB_430833) and Jackson Immunoresearch Lab (goat anti-mouse HRP conjugate, Cat. # 115-035-174, RRID: AB_ 2338512).

Coomassie (Bradford) Protein Assay Kit (Cat. # 23200), Pierce™ BCA protein assay kit (Cat. # 23225) and Supersignal™ West Pico Chemiluminescent substrate (Cat. # 34080) were obtained from ThermoFisher Scientific. Fatty acid free BSA (Cat. # A7030, CAS: 9048-46-8), Triton™ X-100 (Cat. # T9284), sodium dodecyl sulfate (SDS) (Cat. # L3771, CAS: 151-21-3), azide-PEG3-biotin conjugate (Cat. # 762024, CAS: 875770-34-6), methoxypolyethylene glycol maleimide (mPEG) (Cat. # 63187, CAS: 99126-64-4) and N-ethylmaleimde (NEM) (Cat. # E3876, CAS: 128-53-0) were obtained from MilliporeSigma. Tris(2-carboxyethyl)phosphine (TCEP) hydrochloride (Cat. # K831, CAS: 51805-45-9) was purchased from VWR. Tris[(1-benzyl-1H-1,2,3-triazol-4-yl)methyl]amine (TBTA) (Cat. # 18816, CAS: 510758-28-8) was obtained from Cayman Chemicals.

All atom molecular dynamics simulations. We conducted molecular dynamics (MD) simulations of an S-acylated version of a single MLKL protein (PDBID:4BTF) and a membrane model with 600 lipids per leaflet. The membrane was modelled after the PM with a mixture of 5 lipid species, dioleoyl-phosphatidylcholine (DOPC): cholesterol (Chol): dioleoyl-phosphatidylethanolamine (DOPE): palmitoyl-oleoyl-phosphatidylinositol-5-phosphate (POPI-1,5): palmitoyl-oleoyl-phosphatidylinositol-(2,4)-bisphosphate (POPI-2,4) (40:32:20:4:4 mol%). Hereon after, POPI-1,5 and POPI-2,4 are referred to as PIP and PIP2. The model was built using CHARMM-GUI *Membrane Builder* (Lee et al., 2019; Jo et al., 2009), and the protein was acylated with a 24 carbons lipid tail at 280C using the *Solution Builder* and in-house Python scripts. The protein was initially positioned with the 280C residue facing the membrane and the lipid tail partially inserted into the membrane. We ran three simulation replicas of the protein-membrane system with neutralizing ions for 50 ns at 310.15K using GROMACS (Abraham et al., 2015), the CHARMM36m forcefield (Klauda et al., 2010; Huang et al., 2017b; Vanommeslaeghe and MacKerell, 2012), and an integration time of 2fs. In each replica, the membrane lipids started from a different random distribution to ensure independent trajectories. The final configurations of these replicas were transferred to the Anton2 machine (Shaw et al., 2014) to extend the simulation for 1us. The pressure was maintained at 1 bar using the Parrinello-Rahman barostat (Parrinello and Rahman, 1981) with an isothermal compressibility of 4.5×10^{-5} bar^{-1}, and we used the Particle Mesh Ewald methods to account for long range electrostatics (Darden et al., 1993).

Cell culture and culture conditions. Human colorectal adenocarcinoma HT-29 cell (ATCC® HTB-38™, adult Caucasian female origin) were cultured at 37ºC in 5% CO_2 atmosphere in DMEM supplemented with 10% (v/v) fetal bovine serum and 1% (v/v) penicillin/streptomycin solution. Cells were cultured for approximately 2 months and were routinely checked for mycoplasma

infection. Cells were plated according to the requirement of each experiment as described below. Knockdown of zDHHC5, zDHHC20 and zDHHC21 in HT-29 cells was performed as described previously (Parisi et al., 2017). For knockdown, cells were transduced with lentiviral particles packaged with shzDHHC5, shzDHHC20, shzDHHC21 and shRFP in pLKO.1-Puro vector and stably transduced cells were selected with puromycin. For overexpression, commercially available pLYS1-Myc vector was used and subcloned to overexpress MLKL. Lentiviral particles of overexpression system of MLKL and MLKL mutants were packaged similarly as for knockdown.

METHOD DETAILS

Necroptosis treatment. To induce necroptosis cell death, HT-29 cells were initially sensitized to TNF-dependent cell death pathway by SMAC mimetic BV6 (1 μM), and were co-treated with pan-caspase inhibitor zVAD-FMK (25 μM) and incubated for 30 min at 37ºC. Cells were then treated with TNF-α (10ng/mL) and was incubated for 3 h.

(*R*)-MG132 treatments. $8x10^6$ HT-29 cells were plated in overnight. Cells were pretreated with 10 μM of (*R*)-MG132 in DMSO solution for 24h, followed by with BV6, zVAD-FMK and TNF-α treatment. Cells were collected after 3h of necroptosis and ultracentrifuged at 100,000 rcf for 45 min at 4ºC to separate the cytosolic proteins from the membrane proteins. The cytosolic proteins were precipitated using cold 1x PBS, ice-cold methanol and ice-cold chloroform in a 1:2:1.5 ratio and samples were normalized based on protein content. Samples were prepared for Western blotting and 5 μg of sample was loaded for each protein of interest.

Cycloheximide treatments. $1.5x10^6$ HT-29 cells were plated in 6-well plates overnight. Cells were treated with 300 μg/mL cycloheximide (CHX) in DMSO solution along with BV6 and zVAD-FMK 30 minutes prior to addition of TNF-α. Cells were collected at 0, 3 and 5h following necroptosis inducted, lysed and normalized based on protein content. Samples were prepared for Western blotting and 5 μg of sample was loaded for each protein of interest.

Propidium iodide (PI) uptake. Cells ($40x10^3$) were seeded in 96-well plates overnight. After the designated time, the plate was centrifuged for 2 min at 200 rcf at room temperature. The media was removed from each well and 200 μL of 5 μg/mL PI in 1x PBS solution. The plate was incubated for 30 minutes and again centrifuged. The fluorescence was read at the excitation wavelength of 535 nm and emission wavelength of 625 nm in a Biotek Synergy H1 monochromator.

Preparation of extracellular vesicles. Media from the plated shRFP and shzDHHC21 control and necroptotic cells was collected and centrifuged at 300 rcf followed by 800 rcf for 30 mins at 4ºC to remove cell debris. The supernatant was then filtered through a 0.2 µm filter followed by centrifugation at 100,000 rcf for 2h. The media was decanted and the pellet of extracellular vesicles was lysed followed by normalization based on protein content. The samples were then prepared for Western blotting.

Generation of MLKL mutants. The point mutations in the pLys1-MLKL-Myc plasmid were conducted using the QuikChange II XL Site-Directed Mutagenesis Kit (Agilent Technologies Cat# 200521). XL-10 Gold ultracompetent cells were used for transformation and mutated plasmids were extracted using E.Z.N.A® Plasmid DNA Mini Kit. The mutations were confirmed by Sanger sequencing using Genewiz (Azenta Life Sciences). The primers for introducing point mutations were designed on Benchling and obtained from Integrated DNA Technologies. Sequences of primers used to introduce point mutations are provided in Table S2.

Acyl-Peg Exchange (APE). APE procedure was modified based on previous protocols and has been described previously.(Pradhan et al., 2021)

Digital droplet PCR (ddPCR). Total RNA from shzDHHC5, shzDHHC20, shzDHHC21 and shRFP cells was extracted using the E.Z.N.A Total RNA kit. RNA was converted into cDNA using a Biorad Droplet Digital PCR QX200 system with a Biorad iScript cDNA synthesis kit. cDNA was diluted 1:20 for further use with molecular grade water. Reaction mixtures for ddPCR including the primers and cDNA were prepared with ddPCR Supermix for probes according to Biorad protocols and distributed in 96-well plates. A Biorad automated droplet generator was used to create water-oil emulsion droplets in a 96-well plate and subjected to PCR. The cycle was as follows: 95 ºC for 10 min, followed by 40 cycles of (1) 94 ºC for 30 s, (2) 56 ºC for 60 s, with a final 10-min inactivation step at 98 ºC. The plate was read using a QX200 droplet reader, which measured and quantified the fluorescence from the FAM fluorophore of the amplified target gene and the HEX fluorophore of the reference gene (HPRT1). Biorad Quantasoft software was used for data analysis and visualization of the data. The changes in gene expression and *p* values were calculated relative to HPRT1. The sequences for primers and probes are provided in Table S3.

Western Blotting. Samples were loaded and separated with sodium dodecyl sulfate polyacrylamide gel (8% or 10%) electrophoresis at 150 V. Methanol activated polyvinyl difluoride (PVDF) membranes were used. The separated proteins were transferred onto the PVDF membranes at 50 V for 2 hours. Blocking conditions were incubation with 10% non-fat dry milk in

tris-buffered saline (TBS)-Tween [10 mM Tris-base, 100 mM NaCl, 0.1% Tween 20 (pH 7.5)] at room temperature for 1 hour. Membranes were washed four times at 7 minute intervals in TBS-Tween. The corresponding membranes were incubated overnight at 4ºC with primary antibodies (1:500/1:1000 for Myc-tag, 1:2000 dilution for MLKL, 1:500 for pMLKL, 1:10000 for flotillin 1, 1:10000 for calnexin, 1:5000 for α-tubulin). After incubation, the membranes were then washed four times with TBS-Tween for 10 minute each time. Dilutions for anti-rabbit and anti-mouse secondary antibodies were 1:2000 in 5% non-fat dry milk in TBS-Tween, followed by incubation at room temperature for one hour. The membranes were washed as earlier followed by developing with Super Signal West Pico kit.

Quantification of western blots. Fiji software was used for the quantification of Western blots. Samples for all Western blot quantifications were loaded in triplicate. A frame for measurement was developed by using the rectangle tool of Fiji to cover the largest band of the protein of interest. The intensity of the other protein bands was similarly obtained. The background was also measured with the same frame to obtain background intensity measurements. The measured intensities from the protein of interest and background were then inverted by deducting measurements from 255. 255 is the pixel value assigned to white background. The inverted intensities of the protein bands of interest were corrected with the inverted intensities of the background. For APE blots, the relative intensities were obtained by dividing the corrected intensities of migrated bands by that of the non-migrated bands. For all other Western blots, the relative intensities were obtained by dividing the corrected intensity of MLKL or pMLKL to the corrected intensity of the loading control such as calnexin or tubulin. The calculations for every quantification have been described in the respective figure legends.

QUANTIFICATION AND STATISTICAL ANALYSIS

All statistical analysis for the western blot quantifications, cell viability experiments and proteomics were performed using unpaired Student's *t*-test. *p* values and numbers of replicates in all figures are indicated in figure legends, where *** $p < 0.001$, ** $p < 0.01$, * $p < 0.05$, and ns is $p > 0.05$.